SUPERSONIC BIPLANE DESIGN VIA ADJOINT METHOD

A DISSERTATION
SUBMITTED TO THE DEPARTMENT OF AERONAUTICS AND ASTRONAUTICS
AND THE COMMITTEE ON GRADUATE STUDIES
OF STANFORD UNIVERSITY
IN PARTIAL FULFILLMENT OF THE REQUIREMENTS
FOR THE DEGREE OF
DOCTOR OF PHILOSOPHY

Rui Hu

May 2009

I certify that I have read this dissertation and that, in my opinion, it is fully adequate in scope and quality as a dissertation for the degree of Doctor of Philosophy.

(Antony Jameson) Principal Adviser

I certify that I have read this dissertation and that, in my opinion, it is fully adequate in scope and quality as a dissertation for the degree of Doctor of Philosophy.

(Robert W. MacCormack)

I certify that I have read this dissertation and that, in my opinion, it is fully adequate in scope and quality as a dissertation for the degree of Doctor of Philosophy.

(Gianluca Iaccarino)

Approved for the University Committee on Graduate Studies.

Abstract

In developing the next generation supersonic transport airplane, two major challenges must be resolved. The fuel efficiency must be significantly improved, and the sonic boom propagating to the ground must be dramatically reduced. Both of these objectives can be achieved by reducing the shockwaves formed in supersonic flight. The Busemann biplane is famous for using favorable shockwave interaction to achieve nearly shock-free supersonic flight at its design Mach number. Its performance at off-design Mach numbers, however, can be very poor.

This dissertation studies the performance of supersonic biplane airfoils at design and off-design conditions. The choked flow and flow-hysteresis phenomena of these biplanes are studied. These effects are due to finite thickness of the airfoils and non-uniqueness of the solution to the Euler equations, creating over an order of magnitude more wave drag than that predicted by supersonic thin airfoil theory. As a result, the off-design performance is the major barrier to the practical use of supersonic biplanes.

The main contribution of this work is to drastically improve the off-design performance of supersonic biplanes by using an adjoint based aerodynamic optimization technique. The Busemann biplane is used as the baseline design, and its shape is altered to achieve optimal wave drags in series of Mach numbers ranging from 1.1 to 1.7, during both acceleration and deceleration conditions. The optimized biplane airfoils dramatically reduces the effects of the choked flow and flow-hysteresis phenomena, while maintaining a certain degree of favorable shockwave interaction effects at the design Mach number. Compared to a diamond shaped single airfoil of the same total thickness, the wave drag of our optimized biplane is lower at almost all Mach numbers, and is significantly lower at the design Mach number. In addition, by

performing a Navier-Stokes solution for the optimized airfoil, it is verified that the optimized biplane improves the total drag, including the wave drag and the viscous drag, compared to a single diamond airfoil.

Acknowledgments

First and foremost, I would like to express my appreciation to my adviser, Professor Antony Jameson. Without his help, I would not have the chance to pursue my Ph.D degree at Stanford in the first place. He has always been so patient and encouraged me to pursue what I was passionate about throughout my study at Stanford. I deeply enjoy all the conversations with him and I have really learnt a lot from his professional and personal experience.

I would like to express my gratitude to Professor Gianluca Iaccarino. His useful advise about my research is really helpful.

I also thank Professor Robert MacCormack and Professor Juan Alonso. Their aerodynamics and CFD classes not only helped me pass my qualify examination but also greatly prepared me for my research.

I am deeply grateful to Professor Xiaodong Li at Beijing University of Aero & Astro. He introduced me into this wonderful numerical computation kingdom and started my interest in the field.

I have really enjoyed the encouragement and warm company of my friends and colleagues in Aero & Astro and the Aerospace Computing Laboratory. Some of them include Kasidit Leoviriyakit, Georg May, Arathi Gopinath, Sriram Shankaran, Sachin Premasuthan, Jen-Der Lee, Chunlei Liang and Kui Ou. I would also want to thank all my Stanford friends whose names I did not mention here.

Last, and most important, I wish to thank my parents and my husband Qiqi Wang. This thesis would not have been possible without their support. I would like to dedicate this dissertation to them.

Contents

List of Tables

List of Figures

Chapter 1

Introduction

1.1 Supersonic transport

Since the Bell X-1, the first aircraft to exceed the speed of sound in controlled condition, in 1947, a series of military airplanes has been developed to fly beyond the sound barrier. But civil supersonic transport (SST) aircraft designed to transport passengers at speeds greater than the speed of sound have not been so successful. For decades, the speed of commercial aircraft was constrained by the sound barrier. Even with the most successful Concorde, supersonic flight was only available on a small number routes and for those welling and able to pay for the expensive airplane tickets. Compared with a military supersonic strike aircraft, a commercial aircraft have to overcome many of the same challenges, such as an increased lift-to-drag ratio; acceptable takeoff and landing characteristics; highly efficient and durable engines; and advanced materials and structural design. In addition, a commercial aircraft has to meet more environmental constraints than a strike aircraft does. Commercial supersonic flight will only become successful when the technology is matured enough to manufacture aircraft that both satisfy the environmental regulation and are affordable for users in profitably large numbers. According to the report given by the Committee on Breakthrough Technology for Commercial Supersonic Aircraft established by the National Research Council (NRC) [1], three notional commercial supersonic aircraft are defined: a supersonic business jet (SBJ), an overland supersonic commercial

transport, and a high speed civil transport (HSCT) based on customer requirements. These generic aircraft were selected to represent the complete spectrum of supersonic aircraft which are likely to be developed in the foreseeable future.

Among the challenges of supersonic passenger flight, the four most important factors related to economics can be listed as: lift to drag (L/D) ratio, air vehicle empty weight fraction, specific fuel consumption, and thrust-to-weight ratio.

Aerodynamic cruise efficiency is extremely important since it impacts most of the challenges for a viable commercial supersonic aircraft. From the aerodynamics view, the two most important issues are high wave drag and reduced L/D. (Here we define wave drag as the drag caused by the generation of shock waves.) As speeds approach the speed of sound (at about Mach 0.8 to Mach 1.2), the drag coefficient (c_d) will increase up to four times that of subsonic drag. Because of this high wave drag near Mach 1, supersonic aircraft must have considerably more power than subsonic aircraft. To decrease the cruise drag, supersonic vehicles are usually much longer than subsonic aircraft, which in turn tends to degrade low speed performance and increase structural weight. Also, at supersonic speed, the aircraft wing generates lift in a totally different manner than it does at subsonic speed. At about Mach 2, the L/D ratio of a typical wing design is halved (e.g., the Concorde vehicle managed a ratio of 7.14, whereas the subsonic Boeing 747 has an L/D ratio of 17). Because of this reduction of L/D ratio at supersonic speeds, additional thrust is needed to maintain the aircraft's airspeed and altitude, which makes it more difficult to meet community noise standards. In the mean while, the low L/D of the supersonic aircraft increases fuel consumption, limits its range, and increases the design takeoff weight. Regardless of the cruise speed, it is important to increase L/D ratio so that a viable supersonic commercial aircraft is economically viable.

Environmental requirements also result in technical barriers to the development of the new supersonic commercial aircraft. The major environmental concerns include: community noise around airports, sonic boom which prevents supersonic flight over land, climate change, depletion of atmospheric ozone, and local air quality. The huge noise on the ground, known as sonic boom is a big issue that restricts supersonic transport. The sonic boom is a result of the shock wave caused by the aircraft

flying at supersonic speeds. Shock waves, and thus the sonic booms, are unavoidable but can be minimized. Sonic booms can be startling, cause annoyance, and can even result in structural damage. The idea that this huge noise can be avoided by flying higher turned out to be wrong because even when the North American B-70 Valkyrie flew at 70,000ft the noise was still unacceptable high on the ground. Also the Concorde tried to accelerate to supersonic speed over water to avoid the sonic boom over land. But this greatly restricts the wide use of the supersonic commercial aircraft. If one aerodynamic design can be found which reduces sonic booms low enough to gain public acceptance, the economics of supersonic flight would change dramatically. Since the sonic boom is unlikely to be eliminated in the foreseeable future, a more reasonable aim is to produce "shaped" sonic signatures.

For almost 50 years, many countries have conducted commercial supersonic aircraft development programs, which have been marked by intermittent efforts. In the United States, the first major SST Program was terminated in the 1970s before it was finished. In 1985, NASA began the High Speed Research (HSR) Program which was intended "to establish the technology foundation by 2002 to support the U.S. transport industry's decision for a 2006 production of an environmentally acceptable, economically viable, 300 passenger, 5,000 nautical mile, Mach 2.4 aircraft" [6]. The HSR Program was terminated in 1999 mainly because industry showed little commitment to develop such kind aircraft. In fact, even if the HSR Program had been finished, additional fundamental technology and continued research would have been needed to prepare for a real practical commercial transport. In the 1997 National Research Council (NRC) report, the importance of basing SST's performance requirements on the needs of customers, including passengers, airlines, manufacturers, and society, is emphasized. France and Great Britain successfully completed the development of the Concorde. However, after 27 years' service, the last commercial supersonic flight by the Concorde took place in 2003. There are no SSTs in commercial service now.

Today in the busy real world, the requirement to fly faster has created a strong need to develop the next generation of supersonic civil transport which will satisfy both the environmental and economic requirements of low boom and low drag. The ultimate importance of commercial supersonic aircraft to the U.S. air transportation

system is emphasized and set forth in plans by NASA [2], the Department of Transportation [62], and the National Science and Technology Council [58]. Many technical concepts and approaches, although still in their early stage, have been developed [1]. For example, the conceptual laser-propelled aircraft has been developed by Lightcraft Technologies, Inc., and Rensselaer Polytechnic University, partly supported by NASA and the U.S.Air Force [7]. The basic idea of this technology is to use ground-based lasers as aircraft power. Although the key technical problem has been solved, there is still a long way to go before this technology can be used in commercial vehicles. Another example is a technology to downscale the takeoff noise level by injecting some kind of fluid into the engine exhaust. Recently, the Defense Advanced Research Projects Agency (DARPA) Quiet Supersonic Platform (QSP) Program focused their research on smaller supersonic aircraft, while industry (e.g., Gulfstream and Dassault) is exploring the development of a supersonic business jet (SBJ) [13].

1.2 Airfoil Development

As the most important component of the aircraft, the wing produces about two-thirds of the total drag at cruise conditions according to Lynch [45]. The type of operation for which an airplane is intended has a very important bearing on the selection of the shape and design of the wing for that airplane. Therefore, it is a good idea to do more research on the airfoil design problem.

The earliest serious airfoil design efforts began in the late 1800's. Because the early tests of airfoil design were set up under extremely low Reynolds number conditions, thin and highly cambered airfoils were thought to be more efficient. Based on this idea, H.F. Phillips tested a series of airfoil designs in 1884, which were similar in curvature to real bird wings. Otto Lilienthal also experimented with this kind of airfoil. Afterwords, a wide range of airfoils were built by trial and error. In the early 1920's, the famous NACA family airfoils were tested. The first laminar flow airfoil sections, which were originally developed for the purpose of making an airplane fly faster, were designed by Eastman Jacobs at NACA in Langley in 1939. Compared with the conventional airfoil, the laminar flow airfoil is usually thinner, the leading

edge is more pointed and its upper and lower surfaces are nearly symmetrical. After more than one hundred years of effort on airfoil design, even today there is no general rule for airfoil design since every design must be specified according to the flow conditions and the design goals.

For supersonic aircraft, wings with low boom and low drag are preferred. Under supersonic conditions, a strong bow shock wave forms in front of the wing. The bow wave causes an area of very high pressure to form just ahead of the wing, which causes a large increase in pressure drag. One solution to solve this bow shock related high drag problem is using a "supersonic airfoil", which is an airfoil with a very sharp leading edge. By applying this design, the bow wave will attach to the leading edge; thus, the high pressure area ahead of the wing will be eliminated. However, the airfoil with sharp leading edges is very poor in subsonic flight. Therefore, aircraft with very sharp leading edges will have very high stall speeds and are generally unsuited to use as modern airliners because they would require very long runways. If vectored thrust can be used to provide low speed lift in the future, these sharp leading edges may be used on supersonic airliners. Today, it is still an interesting topic what kind of airfoil should be used for supersonic aircraft. The whole problem of drag reduction is an extremely important part of the next generation supersonic transport design.

Considering the drag reduction for three-dimensional wings, more design parameters, such as thickness, camber, twist and sweep, should be combined together to achieve an optimum result. Also, if viscosity is considered, drag reduction should cover the effects of boundary layer friction and drag caused by flow separation. As early as 1960, the idea of using shock wave cancellation to design the supersonic aircraft fuselage was suggested although it was difficult to test at that time. With the increased power of computer-aided design, this idea has become more and more practical. The Shaped Sonic Boom Demonstration (SSBD) program demonstrated successful progress in reducing the intensity of sonic boom by aircraft shaping[55].

Adolf Busemann proposed a supersonic biplane concept in 1935 [5]. For the Busemann biplane, favorable wave interactions are introduce to cancel the strong shock wave between two airfoil elements. Thus, the total wave drag of the biplane is much smaller than that of the monoplane with the same total thickness. Also because the

shock wave is restricted in-between the two elements, the ground noise is decreased a lot. Much research was performed on the Busemann biplane concept from 1935 to 1960's. Moeckel [51] and Licher [41] developed optimized lifting supersonic biplanes by theoretical analysis. Furthermore, Tan [60] calculated analytical expressions for the drag and lift of a three dimensional supersonic biplane with finite span and rectangular planer shape. Ferri [10] obtained some experimental results of the aerodynamic characteristics of the supersonic biplane using the wind tunnel and compared them with the analytical results.

Currently there is renewed interest in supersonic biplane airfoils. Igra and Arad [21] tested different parameters' effect on the drag coefficient of the Busemann airfoil under various flow conditions. Recently, Kusunose proposed using the Busemann's biplane concept to the next generation supersonic transport design. His research group carried out a series of studies including both computational fluid dynamic (CFD) methods and wind tunnel experimental methods ([37, 48, 49, 38, 35, 34]). Figure 1.1 shows a conceptual picture of a Busemann-type boomless supersonic transport based on their biplane concept. They first analyzed the advantages of using biplanes in supersonic flow, and investigated two dimensional Busemann type biplane airfoils in both zero-lift and nonzero-lift conditions by numerical simulation. Furthermore, they proposed a optimized Busemann type biplane via an inverse design method. Then they studied the poor off design aerodynamic performance of the standard Busemann biplane and developed an improved new design by introducing leading edge and trailing edge flaps. They also gave some wind tunnel experimental results to support and compare their CFD results. In 2008, they continued their research on analyzing and comparing several different finite span biplane wings' aerodynamic characteristics. We will discuss biplane airfoil design in detail in Chapter 4.

1.3 Aerodynamic Shape Optimization

In the early years of aerodynamic shape design, the wind tunnel was the primary tool. The configurations of whole aircraft or parts of the aircraft such as the wing were tested and modified by using pressure and force measurement equipment. However,

Figure 1.1: Conceptual drawing of boomless supersonic transport [38]

wind tunnel tests not only cost money, but are also time consuming. Computational methods are now widely used in the aerodynamic design process due to both the radical improvements in numerical algorithms and the rapid increase in modern computer speed and memory.

First, a useful computational method must be based on a mathematical model which should appropriately represent the significant features of the flow, such as shock waves, vortices and boundary layers. Second, the method must be robust and not liable to fail when parameters are varied. Third, the cost of the computational method should be acceptable for a given accuracy level. In the last several decades, many methods have been successfully developed to satisfy all above requirements [52, 3, 29, 33, 54, 56, 46].

By introducing computational methods, a variety of designs can be tested faster and more efficiently. However, the traditional trial and error computational simulation design method does not guarantee the identification of the best possible design. Thus, one has to accept the "best-so-far" design.

This raises the need to introduce optimization theory into the design process. Lighthill [43] first solved a two dimensional incompressible flow design problem by conformal mapping the airfoil profile to a unit circle. In 1979, McFadden [50] further extended Lighthill's method to compressible flow. Another way to design a profile for a given pressure distribution is to integrate the corresponding surface speed to

obtain the surface potential, This approach was first tried by Tranen [61] and has been used to three dimensional design problem by Henne [16]. Garabedian and Korn [11] successfully applied the hodograph transformation to the design of airfoils which produced shock-free transonic flows. The earliest efforts to use constrained optimization were made by Hicks and Henne [18, 17]. First, the configuration is specified by a set of parameters and computational simulation codes are used to calculate the desired aerodynamic characteristics. Then the optimization methods are applied to choose the design parameters so that some criteria, such as minimum drag, will be optimized under given constraints. The major drawback of this method is the large computational cost if the number of design parameters is increased. An alternative is to formulate the design problem using the mathematical theory for the control of systems governed by partial differential equations as developed, for example, by Lions [44]. In this view, the wing is regarded as a device to produce lift by controlling the flow. The shape of the wing is changed to control the flow equations so that the optimal design result is achieved. Suppose that the boundary is defined by a function $f(x)$, where x is the position vector. The design objective is specified by a cost function I, which can be some measures of the wing performance such as drag or lift to drag ratio. A variation in the control δf leads to a cost variation as δI. We will show in the following chapter that δI can be written as an inner product of a gradient function g with δf

$$\delta I = (g, \delta f)$$

Here g can be determined by solving an adjoint equation. If we choose a sufficiently small positive number λ, then

$$\delta I = -\lambda(g, g) < 0$$

assuring a reduction in I. The adjoint based approach significantly decreases the computational cost because the total cost to calculate the gradients is independent of the number of design variables. That is to say the cost is only one flow solution and one adjoint solution. And the adjoint equation is a linear partial differential equation of lower complexity than the flow solution. Jameson [25] first employed the

control theory to transonic design problem. Subsequently, Jameson et al. [26, 31, 32] successfully developed a series shape optimization codes for Euler and Navier-Stokes problems. The adjoint optimization method has been widely applied to varies design problems such as aircraft wing and wing-body configurations [57], wing planform optimization [40] and sail design [59].

1.4 Outline

Chapter 2 describes the governing equations, space discretization, artificial dissipation, multistage time stepping scheme, and convergence acceleration methods used in this research. Chapter 3 formulates the design problem as a control problem and derives the adjoint equation and the corresponding boundary condition for the airfoil inverse design problem under the inviscid condition. Chapter 4 addresses the issue of shock wave drag reduction for supersonic airfoils. Drag reduction and cancellation due to favorable shock wave interference are discussed. Chapter 5 presents the optimization results for inviscid designs for compressible flow based on Busemann biplane airfoil under both zero-lift and lifting conditions. Then the optimized biplane airfoil is validated under viscous condition by solving the viscous flow field of the optimized biplane airfoil directly and also by the flat plates approximation method. Finally, some conclusions and suggestions for future work are presented in chapter 6.

Chapter 2

Governing Equations and Discretization

A multistage scheme is used to find the steady state solution of the flow field. The underlying idea is to integrate the time dependent Euler equations until a steady state is reached. The procedures can be divided into space and time discretization. By subdividing the flow field into polygonal or polyhedral cells, the Euler equations are written in an integral form for each cell, yielding a set of coupled ordinary differential equations. Then, these ODEs can be solved by a multistage time stepping scheme.

2.1 Space Discretization of the Euler Equations

Let p, ρ, u, v, w, E and H denote the pressure, density, Cartesian velocity components, total energy and total enthalpy. For a perfect gas,

$$E = \frac{p}{(\gamma - 1)} + \frac{1}{2}(u^2 + v^2), \quad H = E + \frac{p}{\rho}, \tag{2.1}$$

where γ is the ratio of specific heats. Then, the Euler equations for compressible inviscid flows can be written in an integral form

$$\frac{\partial}{\partial t} \iint_S w dS + \int_{\partial S} (f dy - g dx) = 0 \tag{2.2}$$

for a domain S with boundary ∂S, where w represents the conserved quantities, and f and g represent the fluxes in x and y directions respectively:

$$w = \begin{pmatrix} \rho \\ \rho u \\ \rho v \\ \rho E \end{pmatrix}, \quad f = \begin{pmatrix} \rho u \\ \rho u^2 + p \\ \rho u v \\ \rho u H \end{pmatrix}, \quad g = \begin{pmatrix} \rho v \\ \rho v u \\ \rho v^2 + p \\ \rho v H \end{pmatrix}. \tag{2.3}$$

The computational domain is divided into small subdomains and equation (2.2) is used in each subdomain to determine the flux change in that domain. Here, quadrilateral cells are used and flow variables are stored at the cell centers. Let the values of the quantities associated with each cell be denoted by subscripts i, j. In this way, we will obtain a system of ordinary differential equations (ODEs), which can be written as:

$$\frac{d}{dt}(hw) + Qw = 0, \tag{2.4}$$

where h and Q denote the cell area and the net flux out of the cell, respectively. Let Δx_k and Δy_k be the increments of x and y along side k of the cell, with appropriate signs. Then, we can write the flux vectors for the x momentum component as

$$\frac{\partial}{\partial t}(h\rho u) + \sum_{k=1}^{4}(q_k \rho u_k + \Delta y_k p_k) = 0,$$

where q_k is the flux velocity, defined as

$$q_k = \Delta y_k u_k - \Delta x_k v_k,$$

and the sum is over the four sides of the cell. Each quantity such as u_1 or $(\rho u)_1$ is evaluated as the average of the values in the cells on the two sides of the face,

$$(\rho u)_1 = \frac{1}{2}(\rho u)_{i,j} + \frac{1}{2}(\rho u)_{i+1,j},$$

for example. For a Cartesian grid, the above scheme reduces to the central difference scheme and is second order accurate if the grid is sufficiently smooth.

2.2 Artificial Dissipation

Artificial dissipation was first introduced by Von Neumann and Richtmyer [53]. There are two main reasons to include dissipation terms: to suppress the odd-even point oscillations, and to eliminate oscillations and overshoots around discontinuities and shock waves. When dissipation terms are applied, equation (2.4) can be rewritten as:

$$\frac{d}{dt}(hw) + Qw - Dw = 0 \tag{2.5}$$

where Q is the spatial discretization operator and D is a dissipation operator.

2.2.1 Jameson-Schmidt-Turkel (JST) Scheme

In this research, we use a blended first and third order flux artificial dissipation proposed by Jameson, Schmidt and Turkel [33]. The coefficients of these differences depend on the local pressure gradient.

The dissipative terms for all four dependent variables are constructed in a similar way. Let's take the density equation as an example:

$$D\rho = D_x\rho + D_y\rho$$

where $D_x\rho$ and $D_y\rho$ are corresponding contributions for the two coordinate directions, written in conservation form

$$D_x\rho = d_{i+\frac{1}{2},j} - d_{i-\frac{1}{2},j},$$
$$D_y\rho = d_{i,j+\frac{1}{2}} - d_{i,ji-\frac{1}{2}}.$$

The terms on the right are given in a similar form:

$$d_{i+\frac{1}{2},j} = \frac{h_{i+\frac{1}{2},j}}{\Delta t}\left\{\epsilon^{(2)}_{i+\frac{1}{2},j}(\rho_{i+1,j} - \rho_{i,j}) - \epsilon^{(4)}_{i+\frac{1}{2},j}(\rho_{i+2,j} - 3\rho_{i+1,j} + 3\rho_{i,j} - \rho_{i-1,j})\right\},$$

where h is the cell volume, and the coefficients $\epsilon^{(2)}$ and $\epsilon^{(4)}$ are adapted to the flow.

Define

$$\nu_{i,j} = \frac{|p_{i+1,j} - 2p_{i,j} + p_{i-1,j}|}{|p_{i+1,j}| + 2|p_{i,j}| + |p_{i-1,j}|},$$

then

$$\epsilon^{(2)}_{i+\frac{1}{2},j} = \kappa^{(2)} max(\nu_{i+1,j}, \nu_{i,j}),$$

and

$$\epsilon^{(4)}_{i+\frac{1}{2},j} = max\left(0, (\kappa^{(4)} - \epsilon^{(2)}_{i+\frac{1}{2},j})\right).$$

The typical values of the constants $\kappa^{(2)}$ and $\kappa^{(4)}$ are

$$\kappa^{(2)} = \frac{1}{4}, \quad \kappa^{(4)} = \frac{1}{256}.$$

The dissipation terms for the remaining equations are obtained by substituting ρu, ρv and either ρE or ρH for ρ in these formulas.

2.3 Multistage Time Stepping Scheme

The discretized Euler equations in the last two sections form a set of coupled ordinary differential equations, which can be written as:

$$\frac{dw}{dt} + R(w) = 0, \tag{2.6}$$

where $R(w)$ is the residual and it can be split into two parts:

$$R(w) = Q(w) + D(w). \tag{2.7}$$

Q and D denote the convective part and the dissipative part respectively.

Since we don't care about the details of the transient solution, and the only objective here is to reach a steady state as fast as possible, the time integration schemes with a fast convergence property are chosen. The Runge-Kutta method is a good candidate for our purpose. The classic Runge-Kutta schemes have been successfully applied to a wide range of problems [19, 12, 20, 39]. In this research, we

use a modified Runge-Kutta approach introduced by Jameson [22]. This scheme can be easily used for both structured and unstructured mesh problems [33, 24, 28].

If we denote the time level $n\Delta t$ by a superscript n and the k-th stage by a superscript k, the m-stage Runge-Kutta multistage time-stepping scheme can be written as:

$$\begin{aligned} w^{(n+1,0)} &= w^n, \\ &\cdots \\ w^{(n+1,k)} &= w^n - \alpha_k \Delta t (Q^{(k-1)} + D^{(k-1)}), \\ &\cdots \\ w^{n+1} &= w^{(n+1,m)}, \end{aligned} \tag{2.8}$$

where $\alpha_m = 1$, and

$$\begin{aligned} Q^{(0)} &= Q(w^n), \\ &\cdots \\ Q^{(k)} &= Q(w^{(n+1,k)}), \\ D^{(0)} &= D(w^n), \\ &\cdots \\ D^{(k)} &= \beta_k D(w^{(n+1,k)}) + (1-\beta_k) D^{(k-1)}. \end{aligned}$$

From the above equation, we can see that the convective and dissipative fluxes are treated separately at each stage of the Runge-Kutta scheme in order to extend the stability region along the real and imaginary axises. The coefficients α_k are chosen to maximize the stability of the scheme along the imaginary axis, and β_k are chosen to maximize the stability along the real axis. Actually, the dissipative fluxes don't need to be evaluated at all stages. In this research, a five stage Runge-Kutta scheme

is used, whose coefficients are given as:

$$\begin{aligned}
\alpha_1 &= \tfrac{1}{4}, \quad \beta_1 = 1, \\
\alpha_2 &= \tfrac{1}{6}, \quad \beta_2 = 0, \\
\alpha_3 &= \tfrac{3}{8}, \quad \beta_3 = 0.56, \\
\alpha_4 &= \tfrac{1}{2}, \quad \beta_4 = 0, \\
\alpha_5 &= 1, \quad \beta_5 = 0.44.
\end{aligned}$$

2.4 Convergence Acceleration

Although the invention of faster computers has greatly reduced the computational time, more and more new numerical approaches have been developed to accelerate the solution convergence. In this section, we discuss the three approaches for convergence acceleration used in my research.

2.4.1 Local Time-Stepping

A conservative approach to calculate the time step limit is to evaluate the maximum spectral radius in the whole computational domain and use a global fixed time step which satisfies the limit:

$$\Delta t^*_{ij} = \frac{CFL}{(\bar{\lambda}_\xi + \bar{\lambda}_\eta)_{ij}}, \tag{2.9}$$

where $\bar{\lambda}_{\xi_{ij}}$ and $\bar{\lambda}_{\eta_{ij}}$ are spectral radii of each cell, and CFL is determined by the stability region of the time-stepping schemes. However, this global minimum time-stepping method is very time consuming and not necessary. For viscous problems, the mesh cells near the walls are a thousand to millions times smaller than the mesh cells in the far field. Therefore, by using the local time stepping scheme [22], excessive iterations are avoided and the convergence speed is significantly increased.

In addition to the mesh consideration, the local time stepping scheme also reduces the time step in the high pressure gradient region, which makes the computation more

robust. This local variable time step can be given as:

$$\Delta t_{ij} = \frac{\Delta t^*_{ij}}{(1 + \sigma_\xi + \sigma_\eta)_{ij}},$$

where Δt^*_{ij} is given by equation (2.9), σ_ξ and σ_η are the pressure sensors or normalized second difference of the pressure field in each direction.

2.4.2 Residual Averaging

The residual averaging method, which was introduced by Jameson [27], is used in this research to increase the CFL limit. The basic idea of this method is to replace the residual in one cell in the flow field by a weighted average of the residuals in its neighboring cells. The averaged residual is calculated by an implicit approach which can be given in the following form in the 3D case:

$$(1 - \epsilon_i \delta_{xx})(1 - \epsilon_j \delta_{yy})(1 - \epsilon_k \delta_{zz})\bar{R}_{i,j,k} = R_{i,j,k}, \tag{2.10}$$

where ϵ_i, ϵ_j and ϵ_k are the smoothing controllers, and $\bar{R}_{i,j,k}$ is the averaged residual. The above equation can be easily solved by using a tridiagonal solver in each coordinate direction. A more detailed discussion about the smoothing parameter is provided by Martinelli [47].

2.4.3 Multigrid Methods

The multigrid time-stepping method can effectively accelerate the flow converge to a steady state. The basic idea of a multigrid scheme is to transfer some task of tracking the evolution of the system to a sequence of successively coarser meshes. Thus, the convergence of the total system is accelerated, and the time to obtain the steady state is reduced. The multigrid idea was first proposed by Fedorenko [8, 9], and popularly used for solving elliptic equations by Brandt [4] and Hackbusch [15]. Jameson [23, 24] developed the multigrid scheme to efficiently solve hyperbolic equations.

For a structured mesh in this research, successively coarser meshes can be easily

generated just by eliminating alternate points in each coordinate direction. Suppose 1 to m is used to number the successively coarser grids, where grid 1 is the finest one. First, the solution vector on grid k is initialized as

$$w_k^{(0)} = T_{k,k-1} w_{k-1},$$

where w_{k-1} is the current value on grid $k-1$, and $T_{k,k-1}$ is a transfer operator. For the cell centered scheme used here, the transfer operator is defined as

$$T_{k,k-1} w_{k-1} = \frac{\sum V_{k-1} w_{k-1}}{V_k},$$

where the sum is over the constituent cells on grid $k-1$, and V is the cell area or cell volume. Next, a residual forcing function is transfered such that the solution on grid k is driven by the residuals calculated on grid $k-1$. The forcing function is given as

$$P_k = Q_{k,k-1} R_{k-1}(w_{k-1}) - R_k(w_k^{(0)}),$$

where $Q_{k,k-1}$ is a transfer operator for the fine grid residuals, and can be obtained by summing the residuals in the constituent cells

$$Q_{k,k-1} R_{k-1} = \sum R_{k-1}.$$

Then $R_k(w_k)$ is replaced by $R_k(w_k) + P_k$ in the time stepping scheme. Thus, the modified Runge-Kutta time stepping scheme can be given as

$$\begin{aligned}
&w_k^{(1)} = w_k^{(0)} - \alpha_1 \Delta t_k (R_k^{(0)} + P_k), \\
&\cdots \\
&w_k^{(q+1)} = w_k^{(0)} - \alpha_{q+1} \Delta t_k (R_k^{(q)} + P_k), \\
&\cdots
\end{aligned}$$

The result $w_k^{(m)}$ then provides the initial data for grid level $k+1$. The accumulated correction on grid k has to be transferred back to grid $k-1$. The final value of w_k

is obtained by adding the transfered correction from grid $k+1$ and the correction calculated in the time step on grid k

$$w_k^{new} = w_k + I_{k,k+1}(w_k^{new} - w_k^{(0)}),$$

where $I_{k,k+1}$ is an interpolation operator, and either bilinear or trilinear interpolation is used.

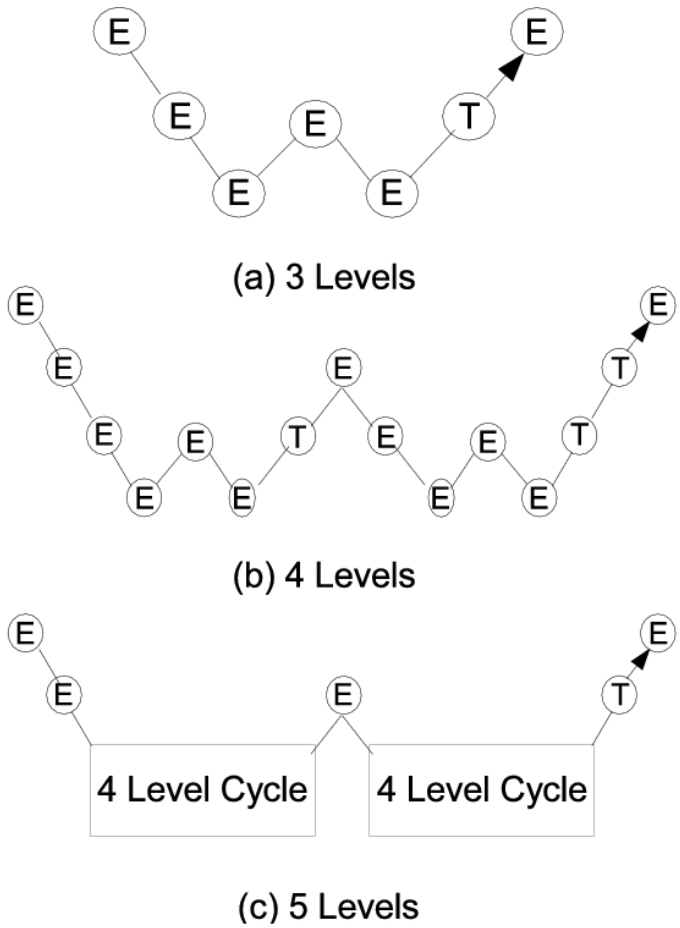

Figure 2.1: Multigrid W-cycle for managing the grid calculation. E, evaluate the change in the flow for one step; T, transfer the data without updating the solution.

With properly optimized coefficients, multistage time-stepping schemes can efficiently drive the multigrid process. The V-cycle is the traditional procedure used to traverse the multigrid levels. However, a W-cycle (as illustrated in Figure 2.1) is often preferred because it manages the work split between the grids more effectively. In a three-dimensional case, the number of cells is reduced by a factor of eight on each coarser grid. From the figure, the total work needed by a W-cycle multigrid step can be written in units corresponding to a step on the fine grid as

$$1 + \frac{2}{8} + \frac{4}{64} + \cdots < \frac{4}{3}.$$

Thus, the large time step of the complete cycle costs only slightly more than a single time step in the fine grid.

Chapter 3

Adjoint Equations and Discretization

3.1 Formulation of the Design Problem as a Control Problem

To apply the optimization method to design problem, a natural approach is to define the geometry via a set of design parameters. For example, the boundary function f can be written as

$$f(x) = \sum \alpha_i b_i(x)$$

where α_i are weights applied to a set of shape functions $b_i(x)$. Then a cost function I, which is also a function of the parameters α_i, is chosen as the drag coefficient or the lift to drag ratio. The sensitivities are calculated by

$$\frac{\partial I}{\partial \alpha_i} \approx \frac{I(\alpha_i + \delta\alpha_i) - I(\alpha_i)}{\delta\alpha_i}$$

where we need to recalculate the flow to obtain the change I. The gradient vector $\frac{\partial I}{\partial \alpha}$ is used to determine a direction of improvement. The simplest approach is to make

a step in the negative gradient direction by setting

$$\alpha^{n+1} = \alpha^n - \lambda \frac{\partial I}{\partial \alpha}$$

so that

$$I + \delta I = I + \frac{\partial I^T}{\partial \alpha} \delta \alpha = I - \lambda \frac{\partial I^T}{\partial \alpha} \frac{\partial I}{\partial \alpha}$$

More sophisticated search procedures may be used such as quasi-Newton methods. Line searches are commonly used to find the minimum in the search direction at each step. The main disadvantage of this approach is the huge computational cost because for each design variable the flow is recalculated to estimate the gradient.

However, using control theory the gradient can be determined by solving a single adjoint equation. The cost of solving the adjoint equation is comparable to that of solving the flow equation. Now the calculation of the gradient becomes independent of the number of design variables and the computational cost is greatly reduced. Here we will give a abstract description of the adjoint method.

A cost function I is chosen such as the drag coefficient or the lift to drag ratio, which is a function of both the flow field variables (w) and the airfoil geometry (represented by the function $\mathcal{F}$). Thus we write it as:

$$I = I(w, \mathcal{F}) \tag{3.1}$$

The change of the cost function due to a change in $\mathcal{F}$ is:

$$\delta I = \left[\frac{\partial I^T}{\partial w} \right]_I \delta w + \left[\frac{\partial I^T}{\partial \mathcal{F}} \right]_{II} \delta \mathcal{F} \tag{3.2}$$

Here, the subscripts I represents the change related to the variation δw in the flow field and II represents the change caused by the shape modification $\delta \mathcal{F}$.

The governing equation R can also be written as function of w and $\mathcal{F}$ within the flow field domain D:

$$R(w, \mathcal{F}) = 0 \tag{3.3}$$

Then δw is determined from the equation

$$\delta R = \left[\frac{\partial R}{\partial w}\right]_I \delta w + \left[\frac{\partial R}{\partial \mathcal{F}}\right]_{II} \delta \mathcal{F} = 0 \tag{3.4}$$

Because the variation δR equals zero, it can be multiplied by a Lagrange Multiplier ψ and subtracted from the variation δI without changing the result. Thus, equation (3.2) can be rewritten as

$$\begin{aligned} \delta I &= \frac{\partial I^T}{\partial w}\delta w + \frac{\partial I^T}{\partial \mathcal{F}}\delta \mathcal{F} - \psi^T \left(\left[\frac{\partial R}{\partial w}\right] \delta w + \left[\frac{\partial R}{\partial \mathcal{F}}\right] \delta \mathcal{F} \right) \\ &= \left\{ \frac{\partial I^T}{\partial w} - \psi^T \left[\frac{\partial R}{\partial w}\right] \right\}_I \delta w + \left\{ \frac{\partial I^T}{\partial \mathcal{F}} - \psi^T \left[\frac{\partial R}{\partial \mathcal{F}}\right] \right\}_{II} \delta \mathcal{F}. \end{aligned} \tag{3.5}$$

where ψ is chosen to satisfy the adjoint equation

$$\left[\frac{\partial R}{\partial w}^T\right] \psi = \frac{\partial I}{\partial w}$$

Now the first term in equation (3.5) is eliminated and δI can be given as

$$\delta I = \mathcal{G} \delta \mathcal{F} \tag{3.6}$$

where

$$\mathcal{G} = \frac{\partial I^T}{\partial \mathcal{F}} - \psi^T \left[\frac{\partial R}{\partial \mathcal{F}}\right]$$

Since equation (3.6) is independent of δw, the gradient of I with respect to an arbitrary number of design variables can be determined without the need to resolve the flow equation. Once the gradient vector $\mathcal{G}$ has been obtained, it may be used to determine the direction of improvement just as we discussed at the beginning of this section.

3.2 Optimization for the Euler and Navier-Stokes equations

We first transform the equations to a fixed computational domain with coordinates ξ_i. This eliminates the need to explicitly include variations of the domain in the variation of the cost function. Suppose we want to minimize the cost function

$$I = \int_{\mathcal{B}} \mathcal{M}(w, S) dB_\xi + \int_{\mathcal{D}} \mathcal{P}(w, S) dD_\xi \tag{3.7}$$

where dB_ξ and dD_ξ denote the surface and volume elements in the computational domain. In general, $\mathcal{M}$ and $\mathcal{P}$ depend on both the flow variable w and the metrics S defining the computational domain. A shape change will cause a variation in the flow solution δw and the metrics δS, which in turn produce a variation in the cost function

$$\delta I = \int_{\mathcal{B}} \delta\mathcal{M}(w, S) dB_\xi + \int_{\mathcal{D}} \delta\mathcal{P}(w, S) dD_\xi \tag{3.8}$$

which can be split in I and II format as

$$\delta I = \delta I_I + \delta I_{II}$$

with

$$\delta\mathcal{M} = [\mathcal{M}_w]_I \, \delta w + \delta\mathcal{M}_{II}$$
$$\delta\mathcal{P} = [\mathcal{P}_w]_I \, \delta w + \delta\mathcal{P}_{II}$$

where we still use the subscripts I and II to distinguish between the contributions associated with the variation of the flow solution δw and those associated with the metric variations δS. Thus $[\mathcal{M}_w]_I$ and $[\mathcal{P}_w]_I$ represent $\frac{\partial\mathcal{M}}{\partial w}$ and $\frac{\partial\mathcal{P}}{\partial w}$ with the metrics fixed, while $\delta\mathcal{M}_{II}$ and $\delta\mathcal{P}_{II}$ represent the contribution of the metric variations δS to $\delta\mathcal{M}$ and $\delta\mathcal{P}$.

In the steady state, the constraint equation specifies the variation of the state

vector δw by

$$\delta R = \frac{\partial}{\partial \xi_i} \delta(F_i - F_{vi}) = 0$$

Here δR, δF_i and δF_{vi} can be split into contributions associated with δw and δS using the notation

$$\begin{aligned} \delta R &= \delta R_I + \delta R_{II} \\ \delta F_i &= [F_{i_w}]_I \, \delta w + \delta F_{iII} \\ \delta F_{vi} &= [F_{vi_w}]_I \, \delta w + \delta F_{viII} \end{aligned}$$

Multiplying by a co-state vector ψ, which will play an analogous role to the Lagrange multiplier introduced in equation (3.2), and integrating over the domain produces

$$\int_{\mathcal{D}} \psi^T \frac{\partial}{\partial \xi_i} \delta(F_i - F_{vi}) d\mathcal{D}_\xi = 0$$

Assuming that ψ is differentiable the terms with subscript I may be integrated by parts to give

$$\int_{\mathcal{B}} n_i \psi^T \delta(F_i - F_{vi})_I d\mathcal{B}_\xi - \int_{\mathcal{D}} \frac{\partial \psi^T}{\partial \xi_i} \delta(F_i - F_{vi})_I d\mathcal{D}_\xi + \int_{\mathcal{D}} \psi^T \delta R_{II} d\mathcal{D}_\xi = 0$$

Since the left hand expression is zero, it can be subtracted from the variation in the cost function (3.8) to give

$$\begin{aligned} \delta I = \delta I_{II} &- \int_{\mathcal{D}} \psi^T \delta R_{II} d\mathcal{D}_\xi - \int_{\mathcal{B}} \left[\delta \mathcal{M}_I - n_i \psi^T \delta(F_i - F_{vi})_I \right] d\mathcal{B}_\xi \\ &+ \int_{\mathcal{D}} \left[\delta \mathcal{P}_I + \frac{\partial \psi^T}{\partial \xi_i} \delta(F_i - F_{vi})_I \right] d\mathcal{D}_\xi \end{aligned} \tag{3.9}$$

Now, since ψ is an arbitrary differentiable function, it may be chosen in such a way that δI no longer depends explicitly on the variation of the state vector δw. The gradient of the cost function can then be calculated from the metric variations without having to recompute the variation δw caused by the perturbation of each design variable.

The variation δw may be eliminated from equation (3.9) by equating all field terms

with subscript "I" to produce a differential adjoint system governing ψ

$$\frac{\partial \psi^T}{\partial \xi_i}\left[F_{iw} - F_{viw}\right]_I + \left[\mathcal{P}_w\right]_I = 0 \quad in\ D \tag{3.10}$$

The corresponding adjoint boundary condition is produced by equating the subscript "I" boundary terms in equation (3.9) to produce

$$n_i \psi^T \left[F_{iw} - F_{viw}\right]_I = \left[\mathcal{M}_w\right]_I \quad on\ \mathcal{B} \tag{3.11}$$

The remaining terms from equation (3.9) then yield a simplified expression for the variation of the cost function which defines the gradient

$$\delta I = \delta I_{II} + \int_{\mathcal{D}} \psi^T \delta R_{II} d\mathcal{D}_\xi$$

substitute the detail expressions of δI_{II} and δR_{II}, we obtain

$$\delta I = \int_{\mathcal{B}} \left\{\delta \mathcal{M}_{II} - n_i \psi^T \delta (F_i - F_{vi})_{II}\right\} d\mathcal{B}_\xi + \int_{\mathcal{D}} \left\{\delta \mathcal{P}_{II} + \frac{\partial \psi^T}{\partial \xi_i} \delta (F_i - F_{vi})_{II}\right\} d\mathcal{D}_\xi \tag{3.12}$$

which only includes the terms containing variations in the metrics while the flow solution is fixed. Hence an explicit formula for the gradient can be derived once the relationship between mesh perturbations and shape variations is defined.

By choosing ψ to satisfy the adjoint equation with appropriate boundary conditions, which depend on the cost function, the explicit dependence on δw is eliminated. Thus the variation of the cost function can be written in terms of δS and the adjoint solution

$$\delta I = \int \mathcal{G} \delta S d\xi =< \mathcal{G}, \delta S >$$

where $\mathcal{G}$ is the infinite dimensional gradient (Frechet derivative) at the cost of one flow solution and one adjoint solution. Then an improvement can be made by setting

$$\delta S = -\lambda \mathcal{G}$$

Although $\mathcal{G}$ can be obtained directly from equation (3.12), the explicit form of equation (3.12) is usually cumbersome to represent. A more compact form can be obtained by integrating the last term of equation (3.12) by parts

$$\begin{aligned}\delta I = &\int_{\mathcal{B}} \left\{\delta \mathcal{M}_{II} - n_i \psi^T \delta (F_i - F_{vi})_{II}\right\} d\mathcal{B}_\xi \\ &+ \int_{\mathcal{B}} n_i \psi^T \left[\delta F_i - \delta F_{vi}\right]_{II} d\mathcal{B}_\xi - \int_{\mathcal{D}} \psi^T \frac{\partial}{\partial \xi_i} \delta \left[F_i - F_{vi}\right]_{II} d\mathcal{D}_\xi\end{aligned} \tag{3.13}$$

The middle terms cancel each other and above equation reduces to

$$\delta I = \int_{\mathcal{B}} \delta \mathcal{M}_{II} d\mathcal{B}_\xi - \int_{\mathcal{D}} \left\{\delta \mathcal{P}_{II} + \psi^T \delta R_{II}\right\} d\mathcal{D}_\xi \tag{3.14}$$

Since equation (3.14) is mathematically equivalent to equation (3.12) but much more compact and easier to program, we used equation (3.14) in our codes.

3.3 Adjoint equation and boundary condition

3.3.1 Inverse Design Problem

An inverse design problem for the inviscid flow is used here to illustrate the basic idea of how to derive the adjoint equation and the corresponding boundary condition. The cost function for this problem is given as

$$I = \frac{1}{2} \int_{\mathcal{B}} (p - p_d)^2 dS \tag{3.15}$$

where p_d is a design pressure distribution we want. Assume that the wing surface is mapped from the physical domain to the computational domain with surface coordinate $\xi_2 = 0$. On this surface,

$$n_1 = n_3 = 0, \;\; n_2 = 1, \;\; d\mathcal{B}_\xi = d\xi_1 d\xi_3$$

The notation S_{ij} represents the projection of the computational ξ_i cell face along the physical x_j axis. Now we can write a wing area vector as

$$S_2 = \begin{Bmatrix} S_{21} \\ S_{22} \\ S_{23} \end{Bmatrix}$$

The cost function (3.15) is transformed to this computational domain

$$I = \frac{1}{2} \iint_{\mathcal{B}_w} (p - p_d)^2 |S_2| d\xi_1 d\xi_3, \tag{3.16}$$

where

$$|S_2| = \sqrt{S_{2j} S_{2j}}$$

denotes the face area corresponding to a unit element of face area in the computational domain. The variation of the cost function (3.16) is given as

$$\delta I = \iint_{\mathcal{B}_w} (p - p_d) |S_2| \delta p d\xi_1 d\xi_3 + \frac{1}{2} \iint_{\mathcal{B}_w} (p - p_d)^2 \delta |S_2| d\xi_1 d\xi_3 \tag{3.17}$$

Since we are considering inviscid condition now, the variation of the constraint equation multiplying by a co-state vector ψ may be written as

$$\int_{\mathcal{B}} n_i \psi^T \delta F_i d\mathcal{B}_\xi - \int_{\mathcal{D}} \frac{\partial \psi^T}{\partial \xi_i} \delta F_i d\mathcal{D}_\xi = 0 \tag{3.18}$$

Here, we assume that the boundary contributions at the far field may either be neglected or else eliminated by a proper choice of boundary conditions. Since the wing is mapped to the $\xi_2 = 0$ surface, all the n_i's equal zero except n_2. Therefore we only need to consider the variation δF_2 for the boundary integral of equation (3.18).

The explicit form of F_2 is given as

$$F_2 = \begin{Bmatrix} \rho U_2 \\ \rho U_2 u_1 + p S_{21} \\ \rho U_2 u_2 + p S_{22} \\ \rho U_2 u_3 + p S_{23} \\ \rho U_2 H \end{Bmatrix}$$

Plugging into the flow tangency boundary condition, $U_2 = 0$, the variation of the inviscid flux at the wing boundary is reduced to

$$\delta F_2 = \delta p \begin{Bmatrix} 0 \\ S_{21} \\ S_{22} \\ S_{23} \\ 0 \end{Bmatrix} + p \begin{Bmatrix} 0 \\ \delta S_{21} \\ \delta S_{22} \\ \delta S_{23} \\ 0 \end{Bmatrix} \tag{3.19}$$

Since equation (3.18) equal zero, it can be simplified and subtracted from equation (3.17). The variation of the cost function now can be given as

$$\begin{aligned} \delta I = & \iint_{\mathcal{B}_w} (p - p_d)|S_2|\delta p d\xi_1 d\xi_3 + \frac{1}{2}\iint_{\mathcal{B}_w} (p - p_d)^2 \delta|S_2| d\xi_1 d\xi_3 \\ & - \iint_{\mathcal{B}_w} (\psi_2 S_{21} + \psi_3 S_{22} + \psi_4 S_{23})\delta p d\xi_1 d\xi_3 \\ & - \iint_{\mathcal{B}_w} p(\psi_2 \delta S_{21} + \psi_3 \delta S_{22} + \psi_4 \delta S_{23}) d\xi_1 d\xi_3 \\ & + \int_{\mathcal{D}} \frac{\partial \psi^T}{\partial \xi_i} S_{ij} \frac{\partial f_j}{\partial w} \delta w d\mathcal{D}_\xi + \int_{\mathcal{D}} \frac{\partial \psi^T}{\partial \xi_i} \delta S_{ij} f_j d\mathcal{D}_\xi \end{aligned} \tag{3.20}$$

To eliminate the flow dependency δw in the domain $\mathcal{D}$ from above equation, ψ should satisfy the adjoint equation

$$\left[S_{ij} \frac{\partial f_j}{\partial w} \right]^T \frac{\partial \psi}{\partial \xi_i} = 0 \ \ in \ \mathcal{D} \tag{3.21}$$

This adjoint equation is linear in terms of ψ and an adjoint boundary condition is needed.

The adjoint boundary condition can be obtained by taking the first and third terms out from the right-hand side of the equation (3.20), which can be written as

$$\psi_2 \frac{S_{21}}{|S_2|} + \psi_3 \frac{S_{22}}{|S_2|} + \psi_4 \frac{S_{23}}{|S_2|} = p - p_d \ \ on \ \mathcal{B}_w \tag{3.22}$$

which is equivalent to

$$\psi_{j+1} n_j = p - p_d \tag{3.23}$$

where n_j's are the components of the surface normal given as

$$n_j = \frac{S_{2j}}{|S_2|}$$

If the adjoint equation (3.21) and the adjoint boundary condition (3.22 are satisfied, the variation of the cost function will not depend on flow variables δp and δw. Equation (3.20) can be reduced to

$$\begin{aligned} \delta I = & \frac{1}{2} \iint_{\mathcal{B}_w} (p - p_d)^2 \delta |S_2| d\xi_1 d\xi_3 \\ & - \iint_{\mathcal{B}_w} p(\psi_2 \delta S_{21} + \psi_3 \delta S_{22} + \psi_4 \delta S_{23}) d\xi_1 d\xi_3 \\ & + \int_{\mathcal{D}} \frac{\partial \psi^T}{\partial \xi_i} \delta S_{ij} f_j d\mathcal{D}_\xi. \end{aligned} \tag{3.24}$$

Same as previous section, above equation can be made more compact by integrating the last term by parts to give

$$\delta I = \frac{1}{2} \iint_{\mathcal{B}_w} (p - p_d)^2 \delta |S_2| d\xi_1 d\xi_3 - - \int_{\mathcal{D}} \psi^T \frac{\partial}{\partial \xi_i} \delta S_{ij} f_j d\mathcal{D}_\xi. \tag{3.25}$$

The gradient of a design parameter $\mathcal{F}$ can be calculated by first perturbing the shape with respect to the parameter $\mathcal{F}$ to produce δS_2 on the boundary $\mathcal{B}_w$ and δS_{ij} in the domain $\mathcal{D}$. Then equation (3.24) or (3.25) is used to calculate the variation of

the cost function δI. The gradient for this design parameter is given as

$$\mathcal{G} = \frac{\delta I}{\delta \mathcal{F}}. \tag{3.26}$$

The same process is repeated for each design parameter. Since the gradient given by equation (3.26) is independent of flow variations, we don't need to recompute the flow equation.

3.3.2 Drag minimization Problem

If we want to minimize the drag of the wing, the drag coefficient is chosen as the cost function

$$I = C_d = \int_{\mathcal{B}} q_i \tau_i dS \tag{3.27}$$

The adjoint equation of drag minimization problem is the same as the inverse problem, which is given by equation (3.21). The form of the adjoint boundary condition depends on the cost function. For the drag minimization problem the adjoint boundary condition is

$$\phi_k = q_k \tag{3.28}$$

3.3.3 Combined Cost Function

Suppose we want to optimize a combined cost function such as a weighted summation of inverse design and drag

$$I = \alpha_1 \cdot \frac{1}{2} \int_{\mathcal{B}} (p - p_d)^2 dS + \alpha_2 \cdot C_D.$$

Because the adjoint equation is linear in ψ and the cost function term only appears at the boundary condition, the adjoint equation for this combined problem is the same as equation (3.21) and the adjoint boundary condition is a weighted linear combination of conditions for the previous two problems.

3.4 Optimization Procedure

Once the gradient has been obtained as described in the previous sections, some optimization algorithm should be chosen to determine the desired shape modification. Linear searches are usually introduced, which is used to find the minimum in the search direction at each step. Two main search procedures [30] have been considered in previous researches.

3.4.1 Simple descent Method

The first is a simple descent method. A small step is taken in the negative gradient direction for each iteration. Let $\mathcal{F}$ represent the design variable, and $\mathcal{G}$ the gradient. Then we can write the iteration

$$\delta\mathcal{F} = -\lambda\mathcal{G}$$

in a pseudo time dependent process as

$$\frac{\mathcal{F}}{dt} = -\mathcal{G}$$

where λ is the time step Δt. This can be analyzed as follows. Let A be the Hessian matrix with elements

$$A_{ij} = \frac{\partial\mathcal{G}_i}{\partial\mathcal{F}_j} = \frac{\partial^2 I}{\partial\mathcal{F}_i\mathcal{F}_j}.$$

Suppose when $\mathcal{F} = \mathcal{F}^*$ a locally minimum value of the cost function $I^* = I(\mathcal{F}^*)$ is obtained. At this point, the gradient $\mathcal{G}^* = \mathcal{G}(\mathcal{F}^*) = 0$ and the Hessian matrix $A^* = A(\mathcal{F}^*)$ must be positive definite. Since $\mathcal{G}^* = 0$, the cost function can be expanded as a Taylor series in the neighborhood of $\mathcal{F}^*$ as following

$$I(\mathcal{F}) = I^* + \frac{1}{2}(\mathcal{F} - \mathcal{F}^*)A(\mathcal{F} - \mathcal{F}^*) + \cdots$$

Correspondingly,

$$\mathcal{G}(\mathcal{F}) = A(\mathcal{F} - \mathcal{F}^*) + \cdots$$

When $\mathcal{F}$ approaches $\mathcal{F}^*$, the leading terms become dominant. Then we can set

$\hat{\mathcal{F}} = \mathcal{F} - \mathcal{F}^*$ and now the search process approximates

$$\frac{d\hat{\mathcal{F}}}{dt} = -A^*\hat{\mathcal{F}}.$$

Also, because A^* is positive definite we can expanded it as

$$A^* = RMR^T,$$

where M is a diagonal matrix containing the eigenvalues of A^*, and

$$RR^T = R^T R = I.$$

Setting

$$v = R^T\hat{\mathcal{F}},$$

the search process can be represented as

$$\frac{dv}{dt} = -Mv.$$

Considering the stability region for the simple forward Euler stepping scheme, which is a unit circle centered at -1 on the negative real axis, we much choose

$$\mu_{max}\Delta t = \mu_{max}\lambda < 2,$$

while the asymptotic decay rate, given by the smallest eigenvalue, is proportional to

$$e^{\mu_{min}t}.$$

3.4.2 Quasi-Newton Method

The second search procedure incorporates a quasi-Newton method for general constrained optimization. The step is defined as

$$\delta\mathcal{F} = -\lambda P\mathcal{G},$$

where P is a preconditioner for the search. An ideal choice is $P = A^{*-1}$, so that the corresponding time dependent process reduces to

$$\frac{d\hat{\mathcal{F}}}{dt} = -\hat{\mathcal{F}},$$

for which all the eigenvalues equal unity. If the Hessian is constant and Δt is set to one, $\hat{\mathcal{F}}$ is reduced to zero in one time step.

Quasi-Newton methods estimate A^* from the change in the gradient during the search process, which requires accurate estimates of the gradient at each time step. Thus, both the flow solution and the adjoint solution should be fully converged. Most quasi-Newton methods also require a linear search in each search direction.Therefore the flow equations and the cost function must be accurately evaluated several times. These methods have proven quite robust in practice for aerodynamic optimization [57], but are computationally expensive.

3.4.3 Gradient Smoothing

Since the gradient $\mathcal{G}$ from previous section is generally less smooth than the shape, in order to make sure that each new shape in the optimization sequence remains smooth it is necessary to smooth the gradient. Also, this smoothing procedure acts as a preconditioner which allows much larger steps. For example, if we want to apply smoothing in the ξ_1 direction, the smoothed gradient $\bar{\mathcal{G}}$ can be calculated from a discrete approximation to

$$\bar{\mathcal{G}} - \frac{\partial}{\partial \xi_1} \epsilon \frac{\partial}{\partial \xi_1} \bar{\mathcal{G}} = \mathcal{G},$$

where ϵ is the smoothing parameter. Then we replace $\mathcal{G}$ by its smoothed value $\bar{\mathcal{G}}$ and set

$$\delta \mathcal{F} = -\lambda \bar{\mathcal{G}}.$$

Then we assume the modification is applied on the surface $\xi_2 =$ constant, the first order change in the cost function is

$$\begin{aligned}
\delta I &= -\iint \mathcal{G}\delta\mathcal{F} d\xi_1 d\xi_3 \\
&= -\lambda \iint \left(\bar{\mathcal{G}} - \frac{\partial}{\partial \xi_1}\epsilon\frac{\partial \bar{\mathcal{G}}}{\partial \xi_1}\right)\bar{\mathcal{G}} d\xi_1 d\xi_3 \\
&= -\lambda \iint \left(\bar{\mathcal{G}}^2 + \epsilon\left(\frac{\partial \bar{\mathcal{G}}}{\partial \xi_1}\right)^2\right) d\xi_1 d\xi_3 \\
&< 0.
\end{aligned}$$

If λ is a sufficiently small positive, above equation will guarantee an improvement until the decent process reach a stationary point at which $\mathcal{G} = 0$.

Conventional optimization methods assume that the design variables are completely independent. However, for our optimization case, the mesh points are used as the design variables, which can not be moved independently due to the shape smoothness requirement. Thus, gradient smoothing is important and necessary. Also, the above optimization algorithm is based entirely on driving the gradient to zero and does not directly measure the cost function. It is possible the gradient could reach zero at a local minimum. For the two dimensional inviscid transonic airfoil optimization problem, however, the drag is almost invariably reduced to zero corresponding to a shock free shape. But the final optimized shape is not unique and depends on the initial shape.

3.5 Discretization of the Adjoint Equations

To solve the adjoint equation (3.21), a pseudo time term is introduced, which will vanish at the steady state. Now we can write the adjoint equation as

$$\frac{\partial \psi}{\partial t} - C_i^T \frac{\partial \psi}{\partial \xi_i} = 0 \ \ in \ \mathcal{D}. \tag{3.29}$$

Comparing to the flow equations, the adjoint equations are linear and not in strong conservation form. Thus we can take adjoint equation as the linearized flow equation but with the reverse propagation wave. The adjoint equations are discretized by the similar techniques as those of the flow equations. Also similar artificial diffusive terms are used for the adjoint equation discretization with the opposite sign.

Chapter 4

Shock Wave Drag Reduction

Based on the physical origins of the drag components, the total drag of a wing can be divided into several components: skin friction drag, wave drag, pressure drag and vortex drag. In supersonic cruise flight, the wave drag, the drag due to the presence of shock waves, is dominant.

4.1 The Wave drag of Supersonic Thin Airfoil

The shock-expansion theory can be used to solve the lift and drag of an airfoil in supersonic flow. If the airfoil is thin and the angle of attack is small, then the lift and drag can be approximately given as simple analytical expressions via the thin airfoil theory [42]. We define the lift and drag coefficients as

$$c_l = \frac{L}{qc}, \;\; c_d = \frac{D}{qc}$$

where L and D are the lift and wave drag of the air foil respectively. And q represents the dynamic pressure, which is

$$q = \frac{1}{2}\rho_\infty U_\infty^2$$

Then according to thin airfoil theory, c_l and c_d for an arbitrary two-dimensional airfoil (as shown in Figure 4.1) can be given as:

$$\begin{aligned} c_l &= \frac{4\alpha_0}{\sqrt{M_\infty^2 - 1}} \\ c_d &= \frac{4}{\sqrt{M_\infty^2 - 1}} \left[\overline{(\frac{dh}{dx})^2} + \alpha_0^2 + \overline{\alpha_c^2(x)} \right] \end{aligned} \tag{4.1}$$

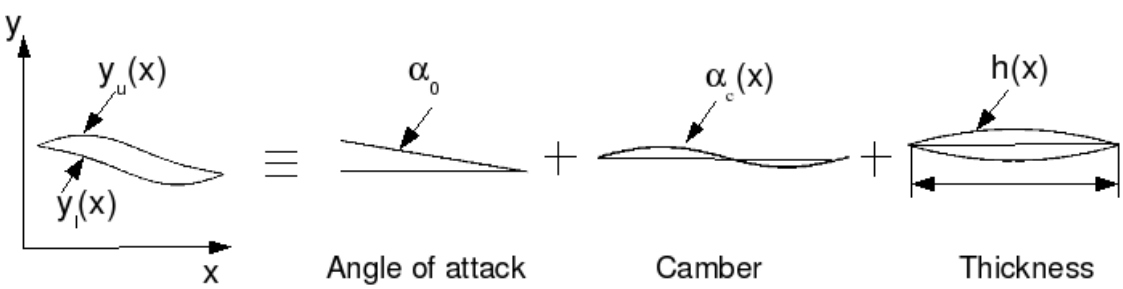

Figure 4.1: Linear resolution of arbitrary airfoil into lift, camber, and drag [42]

From the above equation, it is clear that the lift of this general thin airfoil in supersonic flow only depends on the mean angle of attack. And the wave drag of this airfoil can be split into three parts: drag caused by angle of attack, drag caused by camber and drag caused by thickness. The wave drag in the 2-D case can only be reduced separately according to the different generation mechanism [42].

4.2 Wave Reduction Effect

The drag due to lift (including the drag caused by angle of attack and the drag caused by airfoil camber) can not be eliminated completely. But this part of the drag can be reduced significantly by combining multiple airfoils together [37]. To show this, we first simplify the general airfoil to a flat plate airfoil. Thus c_l is the same as given in

equation (4.1) and c_d is reduced to

$$c_d = \frac{4\alpha_0^2}{\sqrt{M_\infty^2 - 1}} \tag{4.2}$$

We can see clearly that for a flat plate, the lift coefficient is proportional to the angle of attack while the drag coefficient is proportional to the square of the angle of attack.

Considering an airfoil consists of n parallel flat plates with the same chord length c as the single flat plate airfoil, as shown in Figure 4.2. To set the total lift of this n-plates airfoil equal the lift of the single plate airfoil, the angle of attack α_n should be $\alpha_n = \alpha_0/n$. Thus,

$$c_{ln} = n \cdot \frac{4\alpha_n}{\sqrt{M_\infty^2 - 1}} = n \cdot \frac{4\alpha_0/n}{\sqrt{M_\infty^2 - 1}} = c_{ls}.$$

Similarly, the wave drag of this n-plates airfoil equal the summation of the wave drag of each individual plate

$$c_{dn} = n \cdot \frac{4\alpha_n^2}{\sqrt{M_\infty^2 - 1}} = n \cdot \frac{4(\alpha_0/n)^2}{\sqrt{M_\infty^2 - 1}} = \frac{1}{n}\frac{4\alpha_0^2}{\sqrt{M_\infty^2 - 1}} = \frac{1}{n}c_{ds}$$

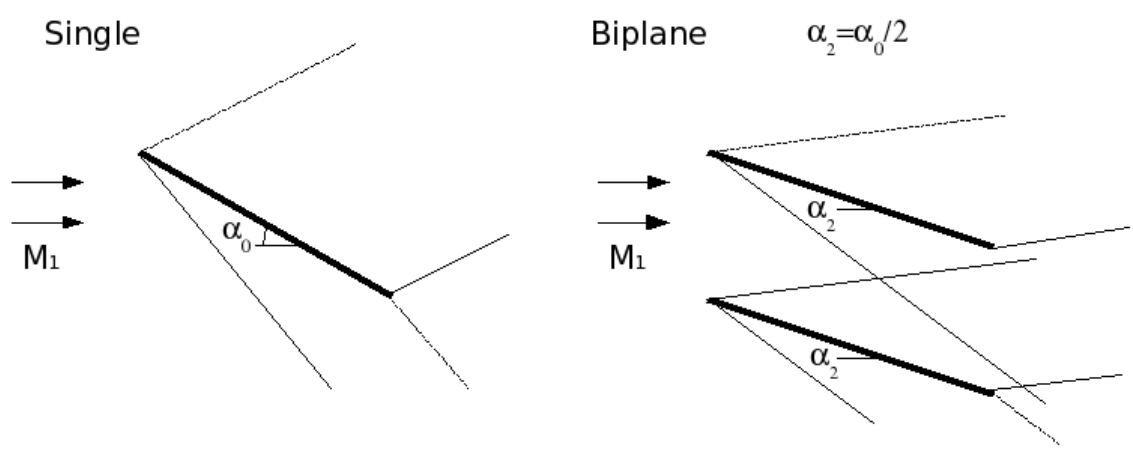

Figure 4.2: Wave reduction effect

From the above equation, we can see that the wave drag of the n-plate airfoil is only $\frac{1}{n}$ of that of a single plate airfoil with the same lift. However, we also should notice that the increased surface area of the multiple airfoil combination will produce more skin-friction drag.

For a multiple airfoil combination configuration, the lift of the individual airfoil will be reduced so that the drag caused by lift will be reduced, while the total lift of the multiple airfoil will not be reduced but only be re-distributed. This is called as the "wave reduction effect" by Kusunose et al in their paper [37].

4.3 Wave Cancellation Effect

The drag due to thickness can be significantly reduced by introducing the biplane configuration. Adolf Busemann [5] proposed a biplane concept by simply dividing a diamond airfoil into two components and placing the triangular surfaces facing each other (Figure 4.4). And by adjusting the distance between the two airfoils at a given Mach number, the strong shock wave generated at the leading edge will exactly reach the inner corner point of the opposite airfoil and will be canceled by the expansion wave at that point. At the design condition, theoretically the shock waves can be completely canceled so that zero wave drag is produced, as shown in Figure 4.3.

However, at design point, because of the entropy increase caused by the shock wave inside the biplane system (as shown in Figure 4.3) and the non-linear effect during the shock-expansion wave interaction processes [42, 14], the zero wave drag condition of the Busemann airfoil design will not be actually realized. Kusunose [36] introduces the Oswatitsch's wave drag expression which can be used to predict this internal shock wave related wave drag. This part of the drag can be given as

$$D_w = P_\infty \int \frac{\Delta s}{R} dz = P_\infty \int \left(-ln \frac{P_0}{P_{0\infty}} \right) dz$$

where, Δs and $\frac{P_0}{P_{0\infty}}$ denote entropy production and the total pressure deficit through shock waves.

At other Mach numbers, the shock wave will only be partially canceled, as shown

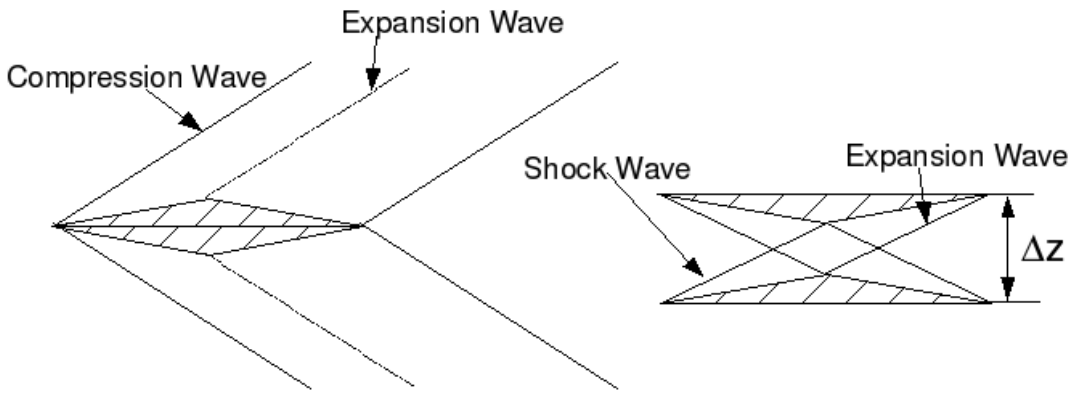

Figure 4.3: Wave cancellation effect

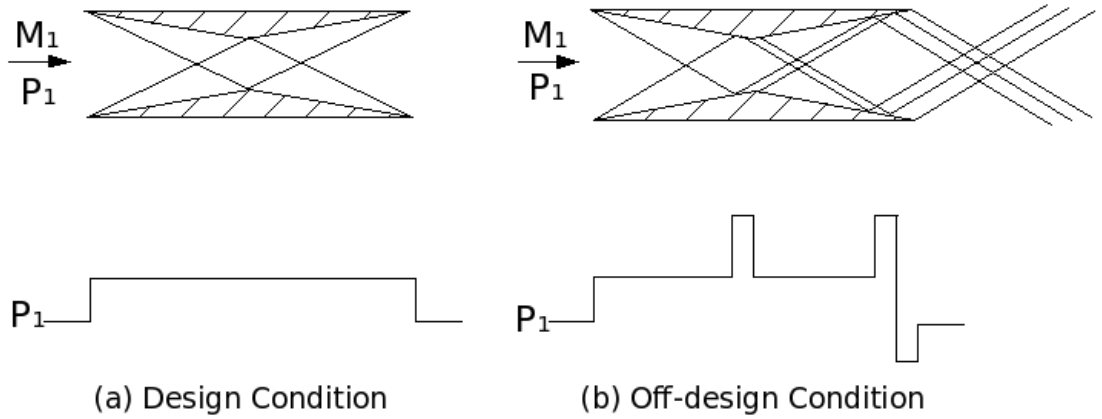

Figure 4.4: Design vs off-design condition of the Busemann biplane

in Figure 4.4. Therefore, the wave drag will not be zero anymore in the off design case.

4.4 Off-Design Condition of the Busemann Airfoil

As discussed above, the Busemann biplane airfoil produces very small wave drag under the design condition. However, under off-design conditions, the Busemann airfoil shows very poor aerodynamic performance. Here, we use computational fluid dynamics (CFD) to demonstrate this. The configurations of the baseline diamond airfoil and the Busemann biplane airfoil are given in Figure 4.5.

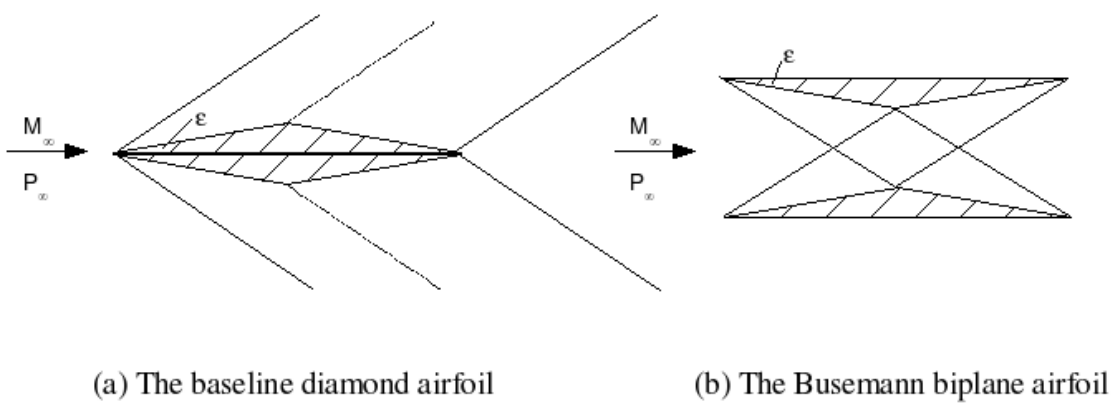

Figure 4.5: Configuration comparison

Figure 4.8 shows the comparison of the drag coefficient(c_d) for these two airfoils over a range of Mach numbers. In these calculations, an impulsive start from uniform flow is used as the initial condition.

As can be seen, when the Mach number is small (lower than 1.6 in the plot), the drag for the Busemann airfoil is higher than that of the diamond airfoil. But in the range of Mach numbers from 1.61 to 2.7, the drag coefficient for the Busemann airfoil becomes lower than that of the diamond airfoil. Especially at Mach number 1.7, which is the design condition for this Busemann airfoil, $c_d = 0.00341$. Due to the favorable shock-shock interaction effect, it is possible for the Busemann airfoil to

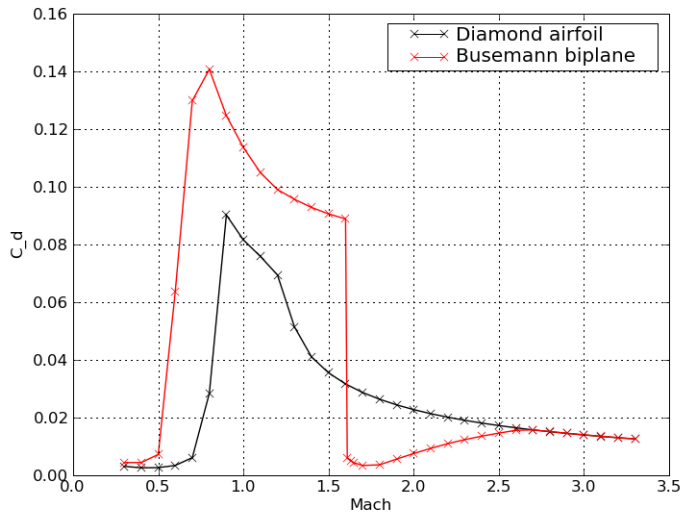

Figure 4.6: c_d plot for different airfoils under zero-lift condition.

produce much smaller drag (the red line in the plot) near the design Mach number than the standard diamond airfoil does. This is the advantage of using the Busemann airfoil design.

These calculations verify that the Busemann airfoil demonstrates very good performance at the design Mach number. But for the off-design conditions, the drag of the Busemann airfoil can be much higher because of the choked-flow phenomenon. Figure 4.7 shows the pressure field around the Busemann airfoil under two different off-design Mach numbers. In the case of $M_\infty < 1.0$, as given in Figure 4.7 (a), the flow becomes sonic at the mid-chord apex and is further accelerated to supersonic. Then a vertical shock wave is formed at the trailing edge of the biplane airfoil. The high wave drag of this Mach number condition is due to the low pressure of the rear part of the airfoil. In the case of $1.0 < M_\infty < 1.6$, as given in Figure 4.7 (a), the flow condition is different. A strong bow shock wave is formed in front of the leading edge and the flow is choked. The flow behind the bow shock wave becomes subsonic and a high pressure field is built so that the wave drag of this off-design condition is also very high.

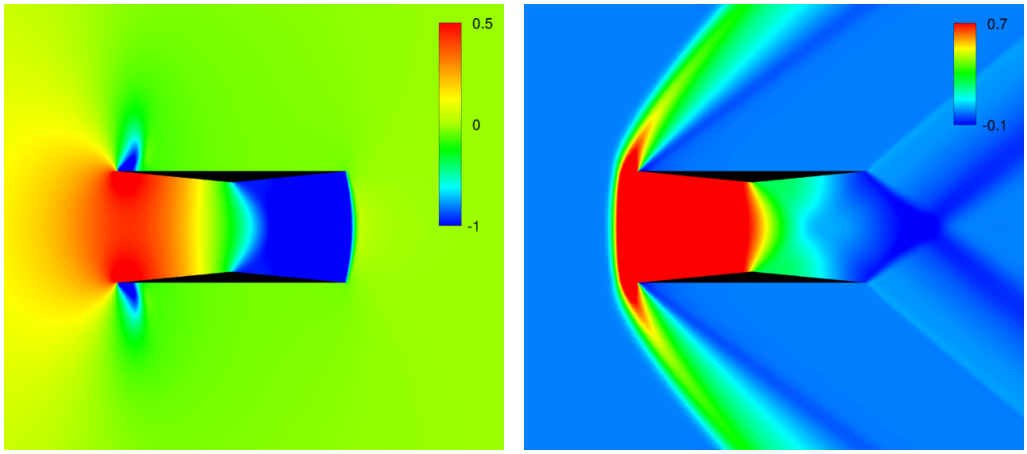

(a) M_∞ =0.8 (b) M_∞ = 1.6

Figure 4.7: Pressure field of the Busemann airfoil under off-design Mach numbers

However, there are even worse problem for the off-design condition of the Busemann airfoil due to the flow-hysteresis phenomenon. If we slowly accelerate the flow by using the previous simulation result as the initial condition, we obtain a new c_d plot versus Mach number as Figure 4.8. From the plot we can see two separated c_d lines in the range near Mach number 1.6 to Mach number 2.1 for the Busemann airfoil. The green line shows the c_d of the Busemann airfoil during acceleration and the red one shows the c_d during deceleration, which are due to the flow-hysteresis phenomenon during acceleration and the choked-flow phenomenon during deceleration. We will discuss them more in Chapter 5.

In order to alleviate the off-design problems of the Busemann airfoil, Kusunose et al [38] proposed a configuration with leading and trailing edge flaps (as given in Figure 4.9).

4.5 Wave Reflection Effect

There is another attractive property of biplane airfoil design. The configuration can be arranged so that the shock wave is reflected to the sky and does not reach the

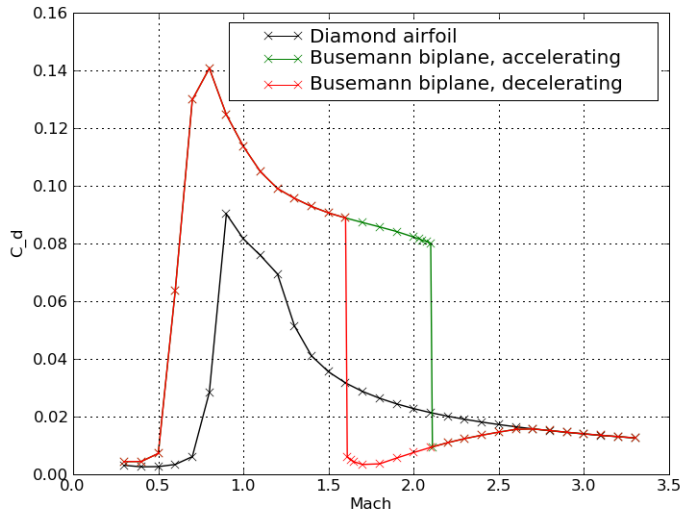

Figure 4.8: c_d plot for different airfoils under zero-lift condition.

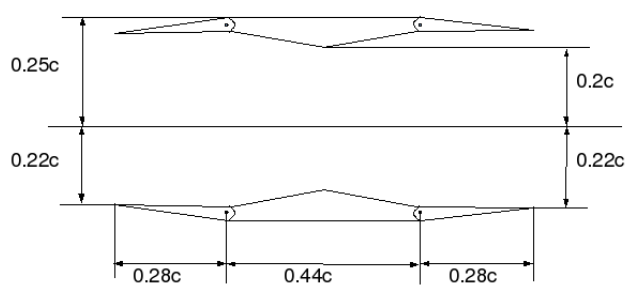

Figure 4.9: Configuration of HLD-1.

ground, and consequently the sonic boom will be dramatically reduced as shown in Figure 4.10.

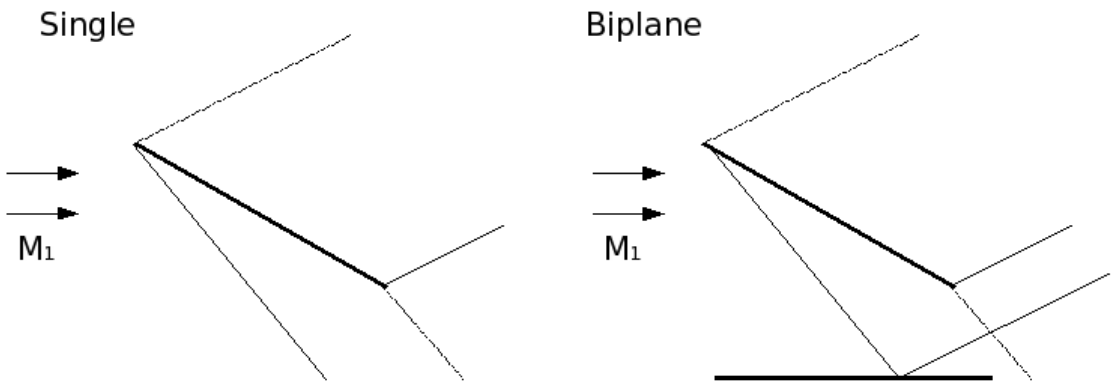

Figure 4.10: Wave reflection effect

However, according to thin airfoil theory, the lift of the biplane system is reduced due to this shock wave reflection. Using CFD Kusunose et al proved in their paper [37], the lift of the biplane system will be zero if all the shock waves are reflected into the sky. Airfoils producing zero lift are not practically useful. Also, because of the poor lift to drag ratio (L/D), as shown in Figure 4.11, the simple shock reflection biplane will not satisfy the low drag and low boom requirements for the supersonic flight.

Liepmann [42] examines several different biplane examples to optimize the ratio D/L^2. Because in a lifting condition, there is a wave drag due to lift, the wave drag of the Busemann biplane is no longer zero. To obtain a beneficial shock-expansion wave interaction, the lift, thickness and camber effects must be considered together.

4.6 Licher's Biplane

Licher [41] has proposed a biplane configuration based on the Busemann biplane idea, which produces relatively higher L/D ratio than the original Busemann biplane. The

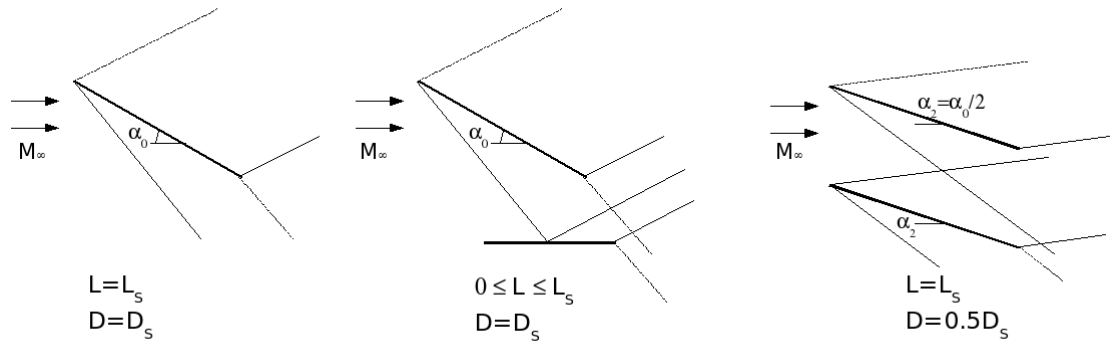

Figure 4.11: L/D ratio reduction due to the wave reflection effect

Licher biplane configuration is shown in Figure 4.12. To produce the same lift, the wave drag caused by lift is only two-thirds of that of a single flat plate due to the favorable wave interactions between the two airfoil components. Meanwhile, similar to the Busemann biplane, the drag caused by the thickness of the Licher biplane is reduced due to the wave cancellation effect.

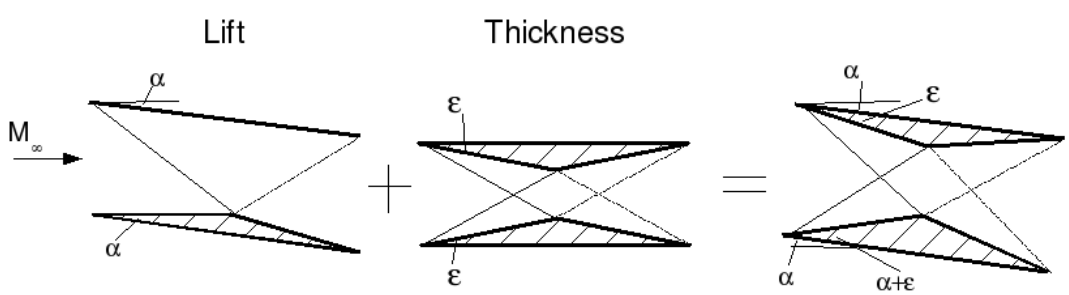

Figure 4.12: Licher's biplane configuration [41]

Chapter 5

Supersonic Biplane Airfoil Optimization Results

This chapter presents the results of multi-point optimization using the design code SYN83. The code includes several modules: the flow solver, adjoint solver, geometry and mesh modification procedures, and the optimization algorithm defined in Chapter 3. In order to treat the biplane configuration we modified the original SYN83 code to use an H-mesh instead of a C-mesh. To check the accuracy of the modified code, we first compare the numerical results, which are calculated by using only the flow solver module, with the analytical results derived from the supersonic thin airfoil theory [42]. Then we show the results we have obtained when the modified codes are applied to optimize the Busemann type biplane airfoil under both zero-lifting and lifting conditions. To test the sensitivity, two cases are studied and we found that the optimized design is robust and not very sensitive to changes in the angle of attack or the separation distance. Finally the design has been validated for viscous flow by solving the Navier-Stokes equations. The results show that the increase in skin friction drag caused by the biplane is generally smaller than the decrease in wave drag. Thus the optimized airfoil obtained by inviscid design tools produces lower total drag than the baseline diamond airfoil in viscous conditions except only for a very small Mach number range during acceleration.

5.1 Code Verification

5.1.1 Original Busemann Airfoil Design

Firstly, the standard diamond airfoil, the separated diamond airfoil and the Busemann airfoil are calculated under the zero-lift condition. To make the results comparable, the total airfoil thickness of these three airfoils are set the same value. Here, the thickness-chord ratio of the diamond airfoil is t/c=0.1, while the thickness-chord ratio of the separated diamond airfoil and the Busemann airfoil are t/c=0.05 for each component. The distance between two Busemann airfoils is set to half of the chord length in order to obtain the theoretical minimum drag for the designed Mach number 1.7. The two components of the separated diamond airfoil are symmetric. The distance between the two components is also set to half of the chord length. The angle of attack of all three airfoils are set to zero.

Figure 5.1 shows the H mesh of the above three airfoils used for calculation. The grid numbers before the airfoil and after the airfoil in the horizontal direction are both 64. In the vertical direction, below and above the airfoil, the grids are also 64. For the separated diamond airfoil and the Busemann airfoil, the grid between the two components is 64×64.

The analytical results obtained by the supersonic thin airfoil theory are given in Table 5.1 and the numerical results calculated by current method are given in Table 5.2. Comparing these two tables, we can see that the numerical results are generally in good agreement with the analytical results. Because of the wave cancellation effect, the wave drag of the Busemann airfoil is much lower than those of other two airfoils. However, we also find that the wave drag of the Busemann airfoil can not be completely eliminated due to the non-linear effect as we discussed in chapter 4.

Next we examine at the detailed conditions for the flow-hysteresis phenomenon during acceleration and the choked-flow phenomenon during deceleration of the Busemann airfoil. Figure 5.2 shows the pressure coefficient of the Busemann airfoil during acceleration. The angle of attack is set to zero and the resulting non-lifting flow field is shown at various supersonic Mach numbers. As can be seen, at Mach numbers up to 2.1, there is a bow shock wave in front of the airfoil. After the bow shock wave,

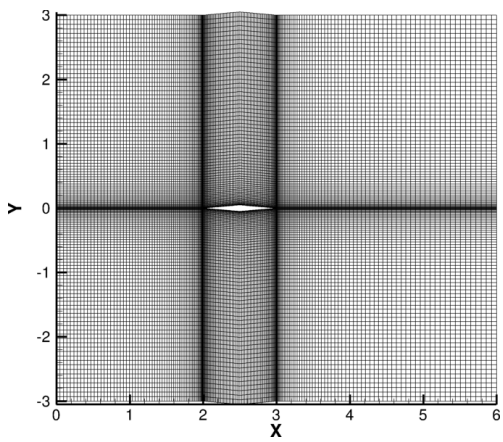

(a) Mesh for standard diamond airfoils

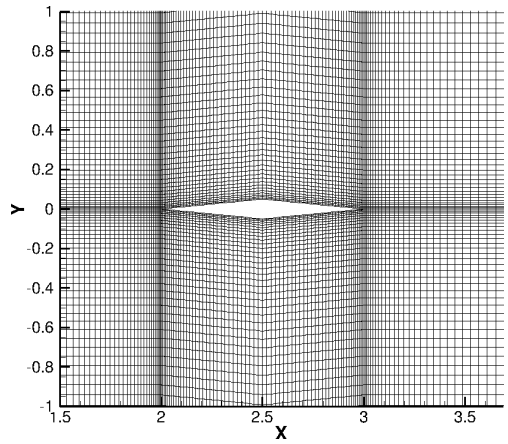

(b) Mesh for standard diamond airfoils zoom in

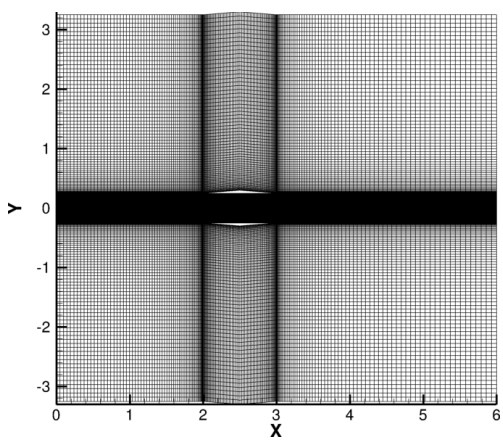

(c) Mesh for separated diamond airfoils

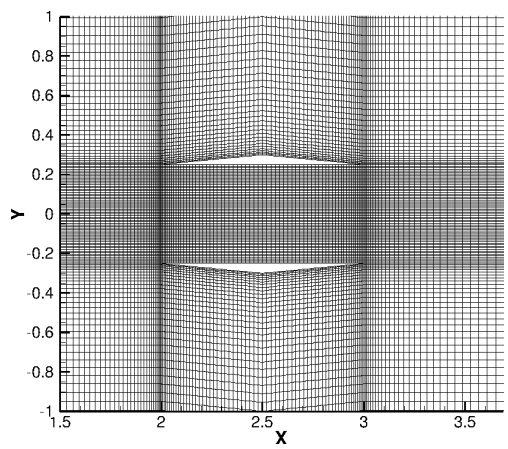

(d) Mesh for separated diamond airfoils zoom in

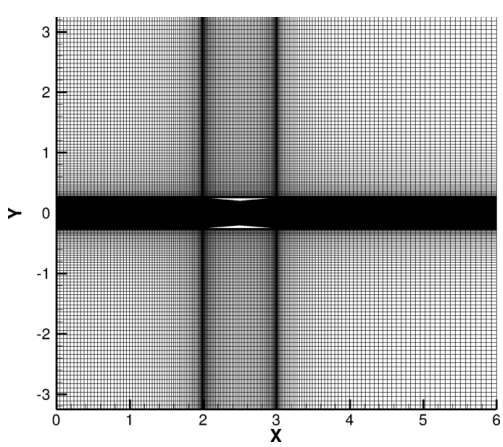

(e) Mesh for Busemann airfoil

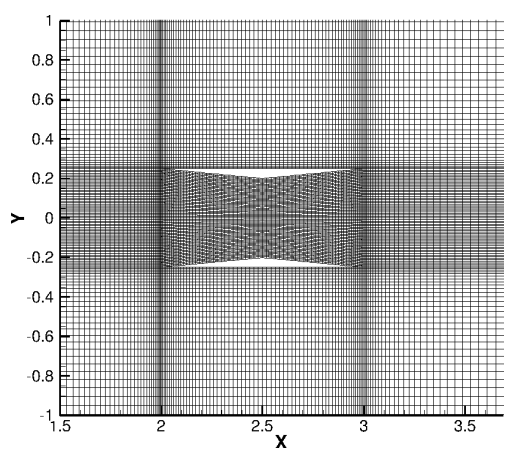

(f) Mesh for Busemann airfoil zoom in

Figure 5.1: Grid configuration for calculation

	c_l	c_d
Diamond airfoil	0.0000	0.0291
Separated diamond airfoil	0.0000	0.0291
Busemann biplane airfoil	0.0000	0.0000

Table 5.1: Theoretical lift and drag coefficients of different airfoils

	c_l	c_d
Diamond airfoil	0.0000	0.0287
Separated diamond airfoil	0.0000	0.0288
Busemann biplane airfoil	0.0000	0.0034

Table 5.2: Numerical lift and drag coefficients of different airfoils

there is a subsonic region between the two airfoils where the pressure coefficient is high (marked by red). This bow shock results in substantially (an order of magnitude) higher drag than in the design condition. When the Mach number increases from 2.1 to 2.11, the bow shock wave is swallowed into the two airfoils and replaced by two oblique shock waves, and the subsonic region between the two airfoils finally disappears. The drag coefficient decreases dramatically and a flow similar to the design condition is obtained. This plot illustrates the poor off-design performance of the original Busemann airfoil. During acceleration, the design condition (c_d = 0.00341) can not be obtained at Mach number 1.7 and the drag coefficient is much higher (c_d = 0.08728). Because of the flow-hysteresis effect, the Busemann airfoil has different c_d during acceleration and deceleration as shown in Figure 4.8.

Figure 5.3 shows the pressure coefficient of the original Busemann airfoil during deceleration. As before, the angle of attack is also set to zero and the resulting flow field is zero-lift. Although the Busemann airfoil shows decent performance in the range near design Mach number, high drag occurs when the Mach number further decreases during deceleration. Because a strong bow shock wave is formed before the airfoil when the Mach number changes from 1.61 to 1.6, the drag increases dramatically from 0.00603 to 0.08886, substantially higher than that of the standard diamond airfoil. The flow is choked at the maximum thickness section and a subsonic area

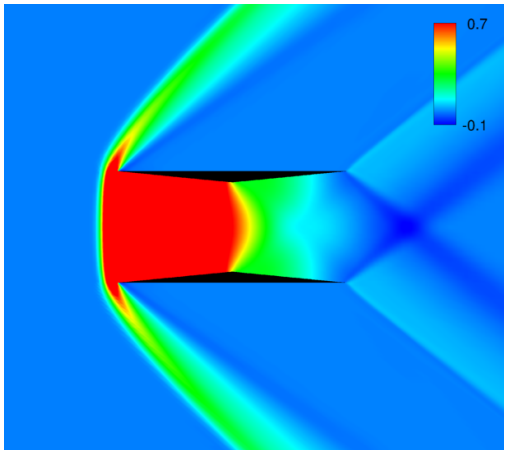

(a) M_∞=1.7,c_d=0.08728

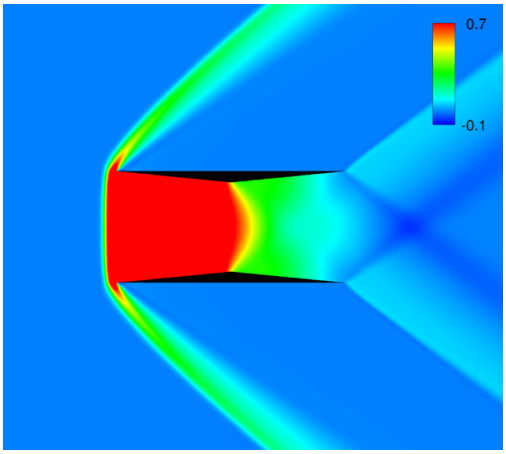

(b) M_∞=1.8,c_d=0.08575

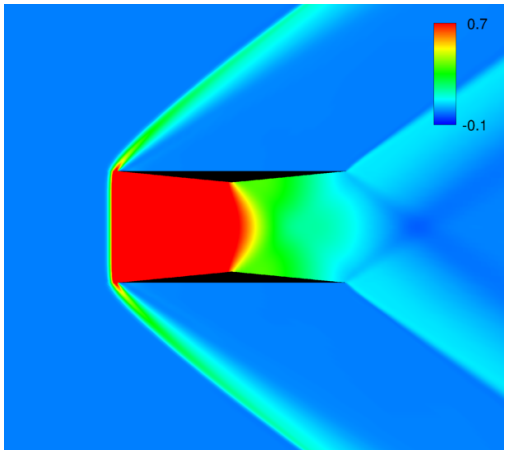

(c) M_∞=1.9,c_d=0.08415

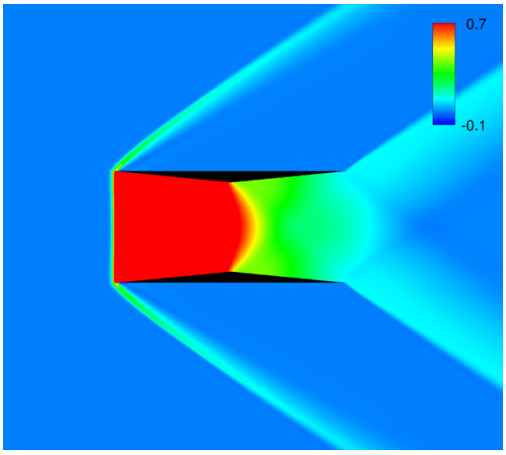

(d) M_∞=2.0,c_d=0.08223

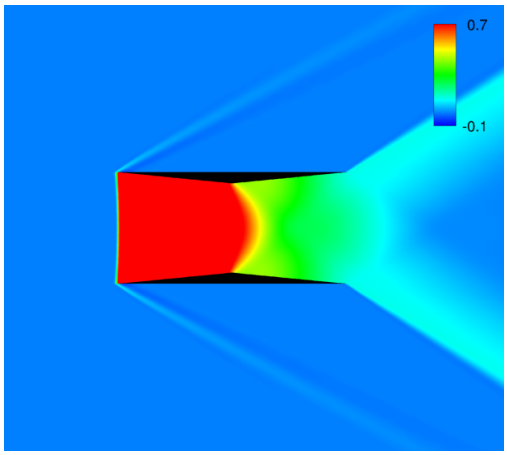

(e) M_∞=2.1,c_d=0.08009

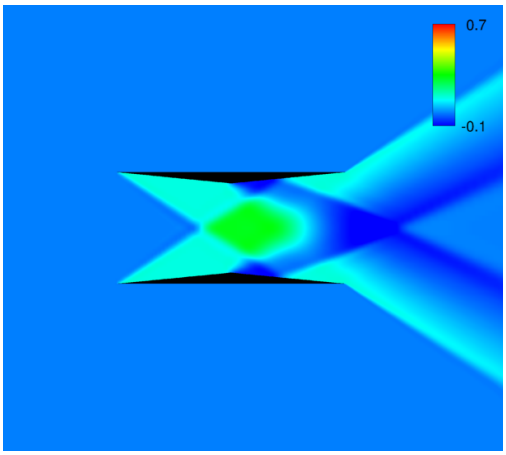

(f) M_∞=2.11,c_d=0.00950

Figure 5.2: C_p-contours of the Busemann biplane with zero-lift during acceleration

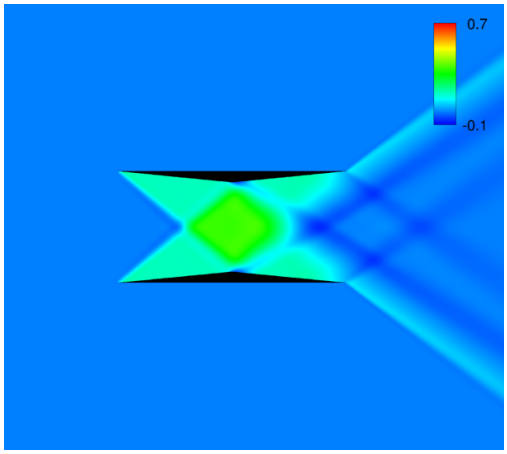

(a) M_∞=1.8,c_d=0.00363

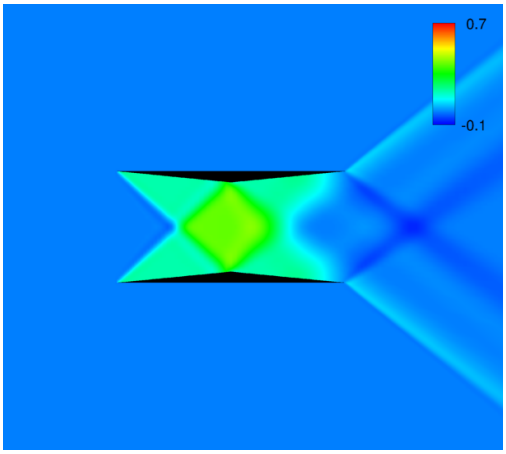

(b) M_∞=1.7,c_d=0.00341

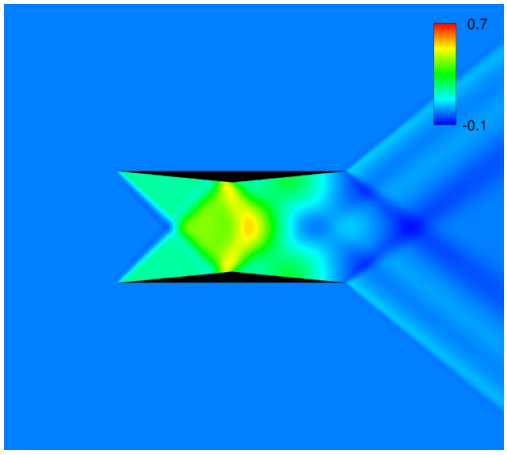

(c) M_∞=1.65,c_d=0.00435

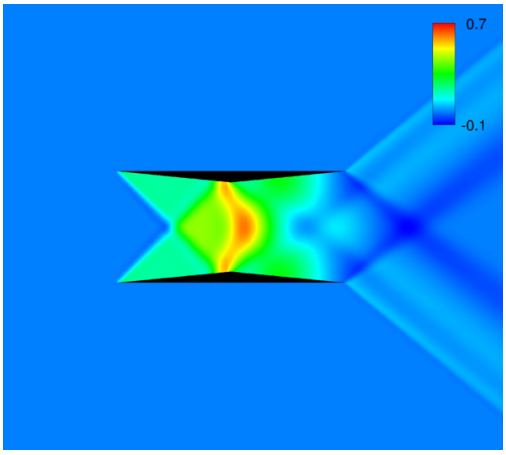

(d) M_∞=1.63,c_d=0.00505

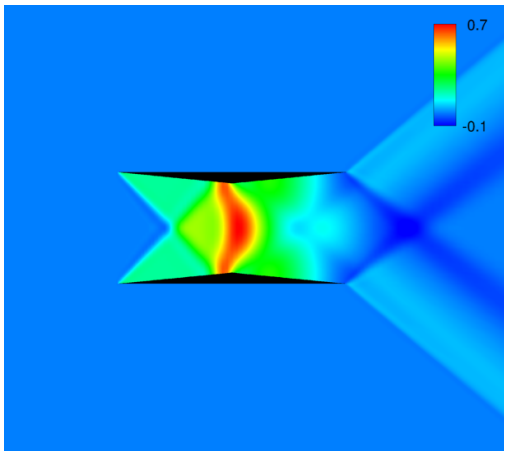

(e) M_∞=1.61,c_d=0.00603

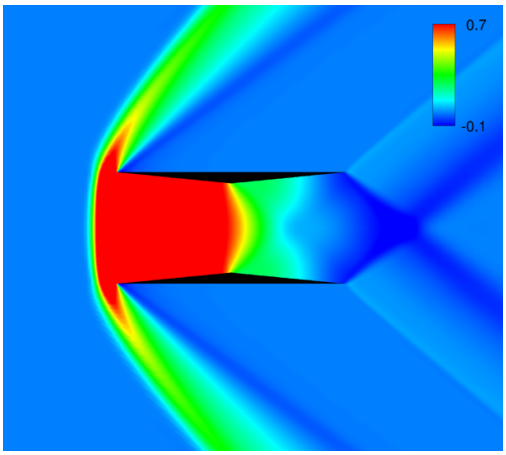

(f) M_∞=1.6,c_d=0.08886

Figure 5.3: C_p-contours of the Busemann biplane with zero-lift during deceleration

is formed. This is also a good demonstration of the poor off-design performance of the Busemann airfoil since the drag of the Busemann airfoil will be greater than the standard diamond airfoil for $M_a \leq 1.6$.

In conclusion, compared to the standard diamond airfoil of the same thickness, the Busemann airfoil produces a higher drag in the low Mach number zone (below the designed Mach number). In addition, we need to accelerate the Busemann biplane to a higher Mach number, while producing higher drag and then decrease velocity to get the design condition. Thus, the Busemann biplane airfoil need to be redesigned so that the high drag zone caused by the flow-hysteresis and choke-flow phenomenon can be avoided or at least reduced.

The separated diamond design is the first biplane design calculated here to avoid the flow-hysteresis and choke-flow phenomenon. Figure 5.4 shows the comparison of drag coefficients of the standard diamond airfoil, the separated diamond airfoil and the Busemann airfoil. The Mach number ranges from 0.3 to 3.3 just as in Figure 4.8. From the plot, we can see that the c_d line of separated diamond airfoil agrees very well with the standard diamond airfoil. In the separated diamond airfoil case, no choke-flow or flow hysteresis phenomenon happened. However, since the separated diamond airfoil shows the same drag characteristics as the standard diamond airfoil, which produces higher c_d at our design condition (Mach number 1.7) than the Busemann airfoil, we hope to optimize the Busemann airfoil by choosing a shape combining Busemann airfoil and the separated diamond airfoil designs.

5.2 Optimized design under Non-lifting Condition

The initial computational grid is shown in Figure 5.1. Multiple design points are used in the optimization process since the original Busemann airfoil showed flow hysteresis and choke-flow phenomenon during acceleration and deceleration. For this multi-point design case, the objective function used here is a weighted average of c_d, which can be written as:

$$I = \sum_{i=1}^{n} w_i I_i \tag{5.1}$$

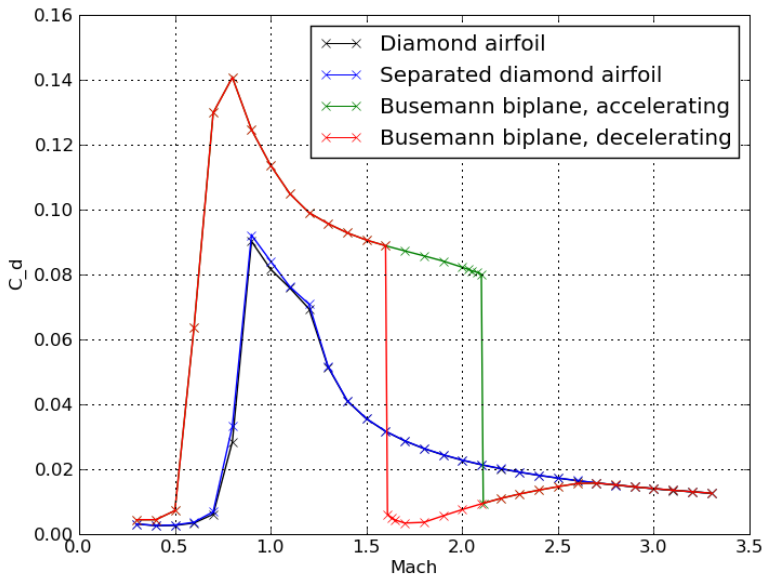

Figure 5.4: c_d plot for different airfoils under zero-lift condition.

Because the wave drag of a biplane airfoil will be much smaller when the flow is unchoked, we want the strong bow shock wave be swallowed before the design Mach number. The multiple design points and the corresponding weight used in this research are given in Table 5.3. Here equal weight is given to each design point. Actually, higher weight could be put on the most important design Mach number to produce lower drag at that point.

Mach	1.1	1.2	1.3	1.4	1.5	1.6	1.7	1.6	1.5	1.4	1.3	1.2	1.1
Weight	$\frac{1}{13}$	$\frac{1}{13}$	$\frac{1}{13}$	$\frac{1}{13}$	$\frac{1}{13}$	$\frac{1}{13}$	$\frac{1}{13}$	$\frac{1}{13}$	$\frac{1}{13}$	$\frac{1}{13}$	$\frac{1}{13}$	$\frac{1}{13}$	$\frac{1}{13}$

Table 5.3: Multiple design points and the corresponding weight

The lift coefficient c_l is fixed to zero and a constant thickness constraint is used during the optimization process. In addition, the points of the maximum thickness section of the Busemann airfoil are fixed so that the optimized airfoil has the same throat area as the original Busemann airfoil.

Figure 5.5 shows the weighted c_d for all design points during the design iterations.

From the plot, we can see the cost function converges in 750 design iterations. Therefore, we use the resulting airfoil after 750 design iterations as our optimized biplane airfoil.

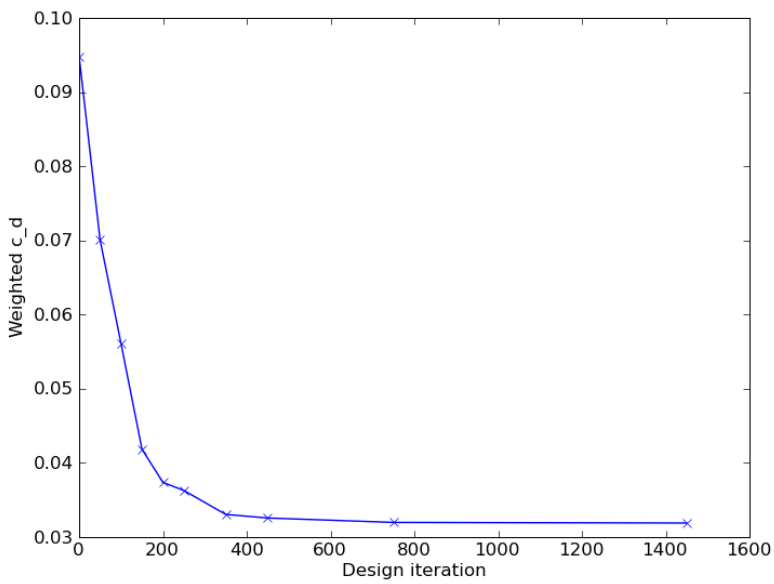

Figure 5.5: Convergence history under zero-lift conditions.

Figure 5.6 shows a comparison of the optimized biplane airfoil with the original Busemann airfoil. We can see that the optimized biplane airfoil has the same thickness as the original Busemann airfoil at all corresponding positions and the thickest position is fixed by the constraints. The wedge angles of these two airfoils are the same. The leading edges and trailing edges of the optimized biplane airfoil bend towards the center. The two components of the optimized biplane airfoil are still symmetric with respect to the Y-axis in Figure 5.6 due to the zero-lift condition.

The drag coefficients for each design point are compared in Table 5.4. From the table, we can see the baseline Busemann airfoil is choked at all Mach numbers in the optimization range, while the optimized biplane is unchoked at a wider range (from 1.6 to 1.7 to 1.4). And even for the choked condition, the optimized biplane airfoil has much lower drag than the baseline Busemann airfoil.

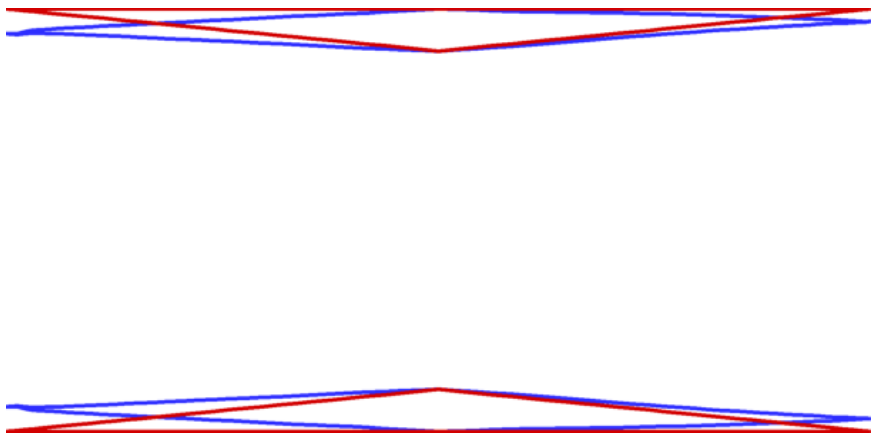

Figure 5.6: Comparison of the baseline Busemann airfoil and the optimized biplane airfoil. The red line indicates the baseline Busemann airfoil; the blue line indicates the optimized biplane airfoil.

Mach	1.1	1.2	1.3	1.4	1.5	1.6	1.7	1.6	1.5	1.4	1.3	1.2	1.1
Baseline	1050	996	957	928	906	889	873	889	906	928	957	996	1050
Optimized	527	473	419	376	332	112	106	112	127	152	419	473	527

Table 5.4: c_d comparison for zero lift condition (1 count = 0.0001)

Figure 5.7 shows the comparison of the drag coefficient for the optimized biplane airfoil with the standard diamond airfoil and the baseline Busemann airfoil. From the plot, we can see there are still two separated c_d lines for the optimized biplane airfoil, which means that the flow hysteresis and choked-flow effect still exist. However, the flow hysteresis area has been greatly reduced. We also found from the plot that the drag increase due to the choked-flow also becomes much smaller than that of the original Busemann airfoil. From the plot, we can see that the drag of the optimized biplane airfoil is also smaller than that of the original Busemann airfoil in the subsonic area (Mach number 0.5 to 0.9) although it is higher than the standard diamond airfoil below Mach number 0.8. Considering both subsonic and supersonic conditions, we see the optimized biplane airfoil greatly reduces the wave drag. At the design condition (Mach number 1.7), the wave drag of the optimized biplane airfoil is higher ($c_d = 0.01064$) than that of original Busemann airfoil ($c_d = 0.00341$). This is because we focused on reducing the choked-flow and flow hysteresis effect in this design and optimized the airfoil for multiple Mach numbers with equal weight. To alleviate this problem, we could put more weight on the design Mach number 1.7 during the optimization process.

We now examine the details of the accelerating and decelerating conditions. Figure 5.8 and Figure 5.9 show the pressure coefficient distribution of the optimized biplane airfoil during acceleration and deceleration respectively. During acceleration (Figure 5.8), the flow hysteresis effect still forms a bow shock wave in front of the airfoil. When the Mach number increases from 1.52 to 1.53 (compared with Busemann at Mach number 2.11), the shock wave is swallowed into the two airfoils and the wave drag decreased greatly from 0.03336 to 0.01221. During deceleration (Figure 5.9), we can also observe that there is also a choked-flow phenomenon. But the optimized biplane airfoil shifts the choked flow at the maximum thickness sections to a lower Mach number (Mach number 1.37 here) than the original Busemann airfoil (Mach number 1.6).

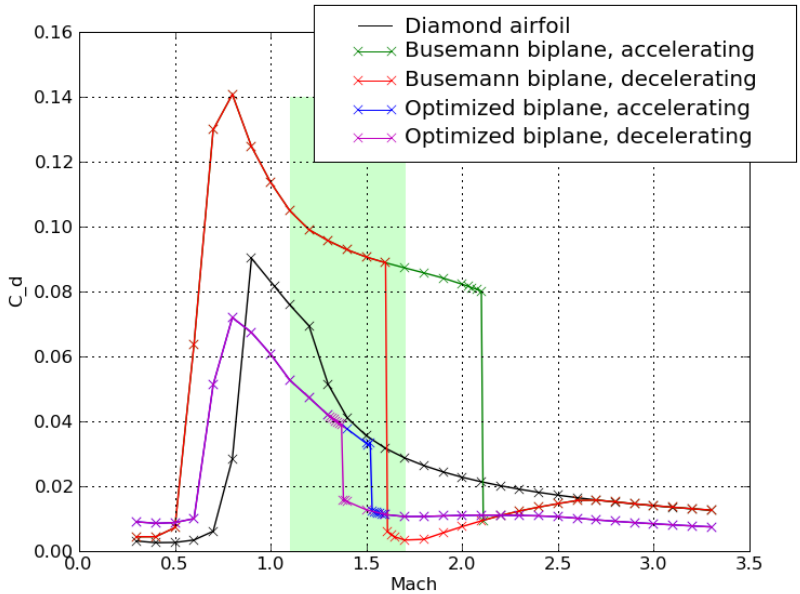

Figure 5.7: c_d plot for different airfoils under zero-lift conditions.

5.3 Busemann Biplane under Lifting Condition

In the real word, we care more about the lifting condition than the zero-lift condition. Here, we apply our optimization method to the lifting condition. Two lifting cases are tested - c_l 0.05 and 0.1. The same number of mesh points and grid configurations are used in all the computations. Figure 5.10 shows the comparison of the drag coefficient of the standard diamond airfoil and the original Busemann airfoil over a range of Mach numbers (0.3 to 3.3) for these two lift coefficients. From the plot, we can see the c_d plot for the Busemann airfoil still splits into two lines, one for acceleration and the other for deceleration in both cases. This split implies flow hysteresis and choke-flow phenomenon. At Mach number 1.7, the Busemann airfoil produces much less wave drag than the standard diamond airfoil does because of the favorable shock-shock interaction effect.

Under both lifting conditions, the bow shock wave in front of the airfoil results in substantially higher drag at high Mach numbers (about 2.08) during acceleration. When the Mach number increases, the bow shock wave is swallowed and the subsonic

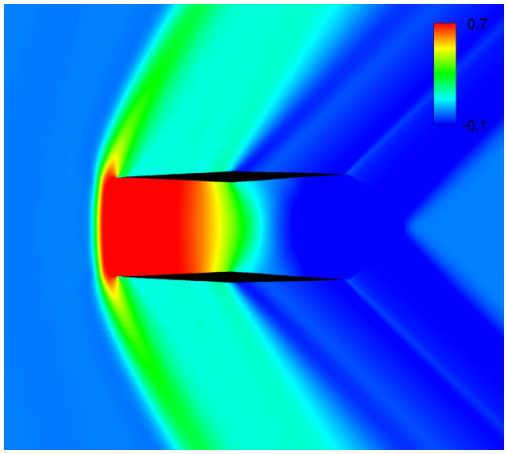

(a) M_∞=1.3,c_d=0.04190

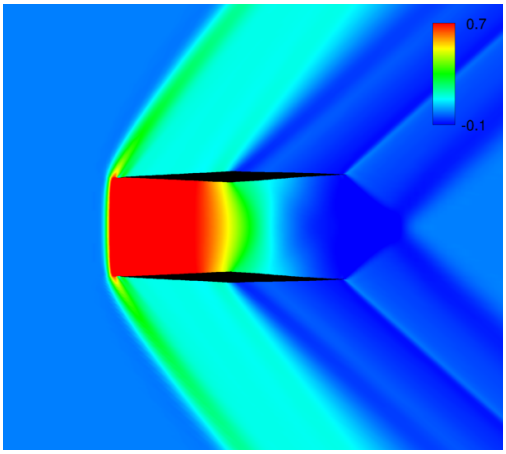

(b) M_∞=1.4,c_d=0.03761

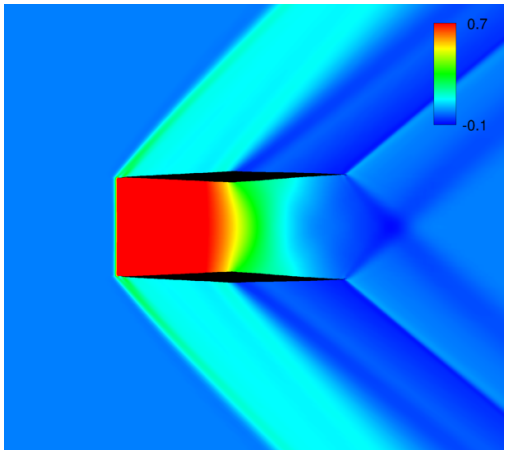

(c) M_∞=1.5,c_d=0.03318

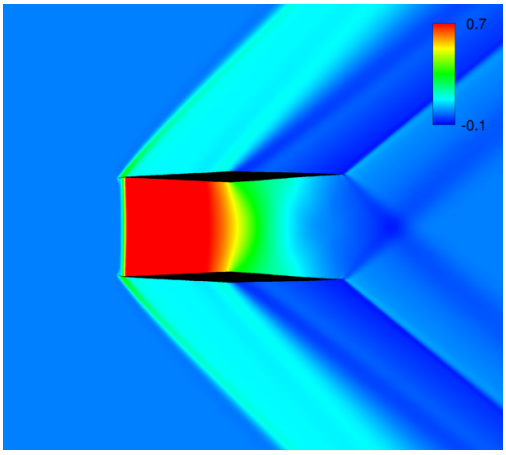

(d) M_∞=1.52,c_d=0.03336

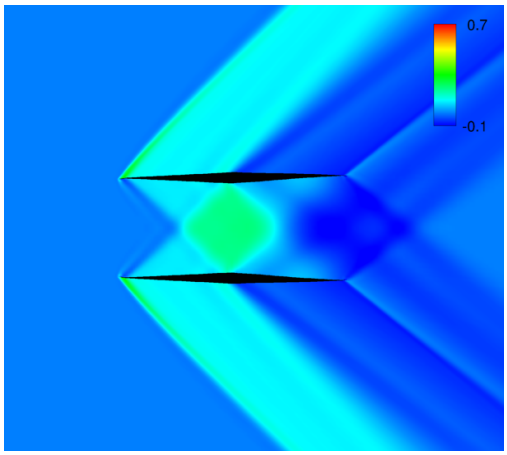

(e) M_∞=1.53,c_d=0.01221

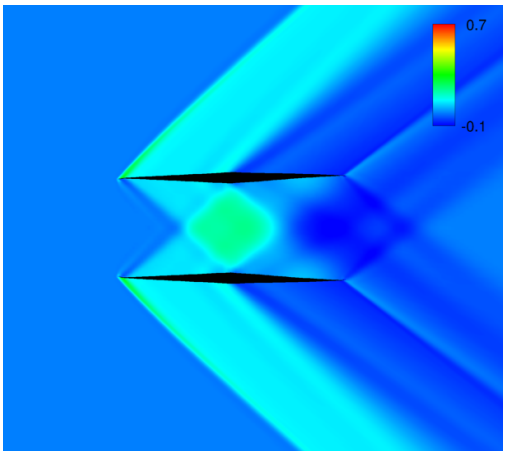

(f) M_∞=1.6,c_d=0.01125

Figure 5.8: C_p-contours of the optimized biplane with zero-lift during acceleration

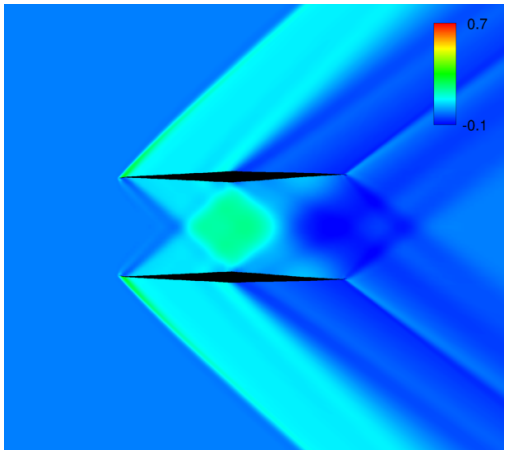

(a) M_∞=1.6,c_d=0.01125

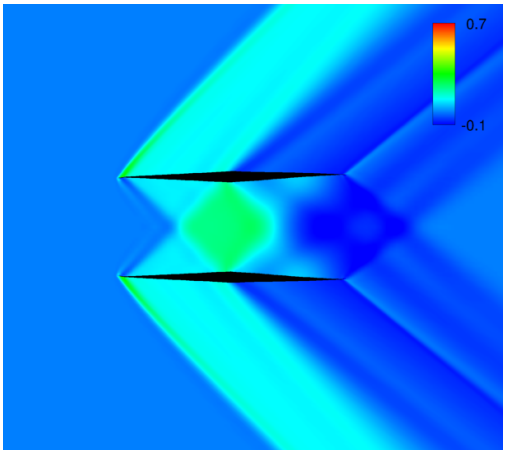

(b) M_∞=1.5,c_d=0.01273

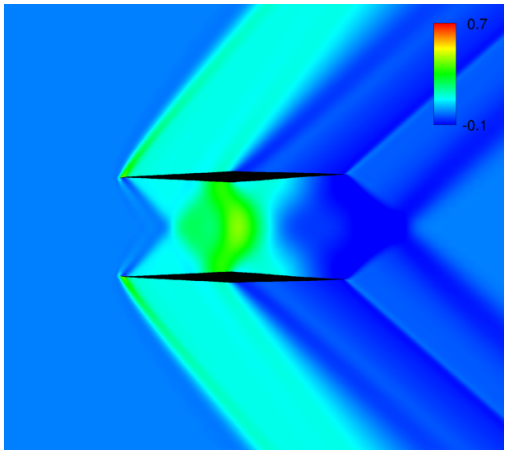

(c) M_∞=1.4,c_d=0.01526

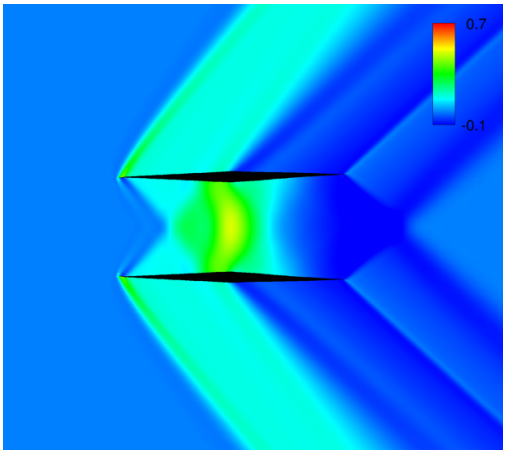

(d) M_∞=1.38,c_d=0.01582

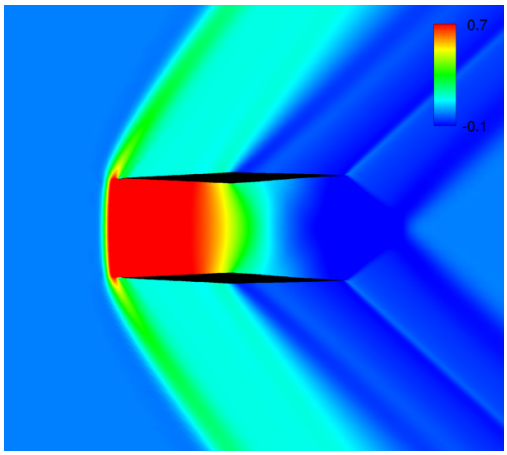

(e) M_∞=1.37,c_d=0.03886

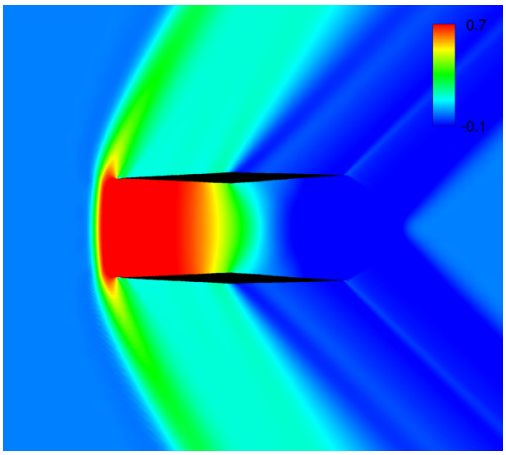

(f) M_∞=1.3,c_d=0.04191

Figure 5.9: C_p-contours of the optimized biplane with zero-lift during deceleration

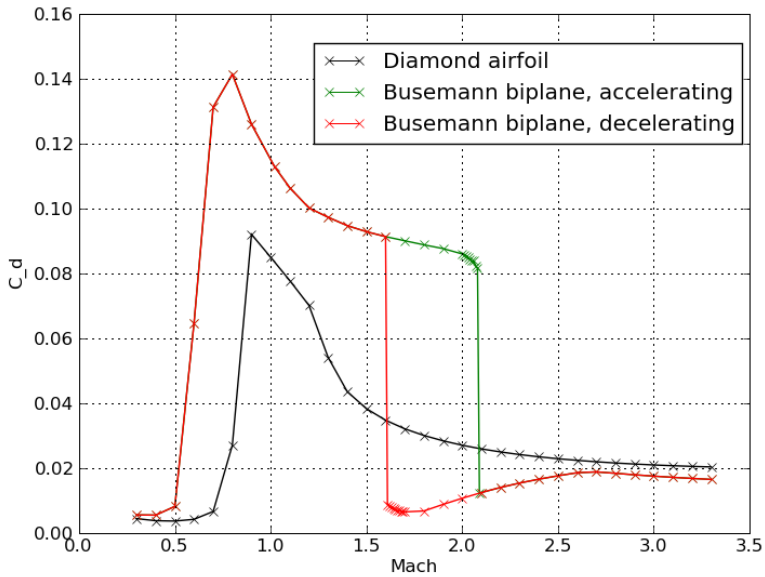

(a) $c_l = 0.05$

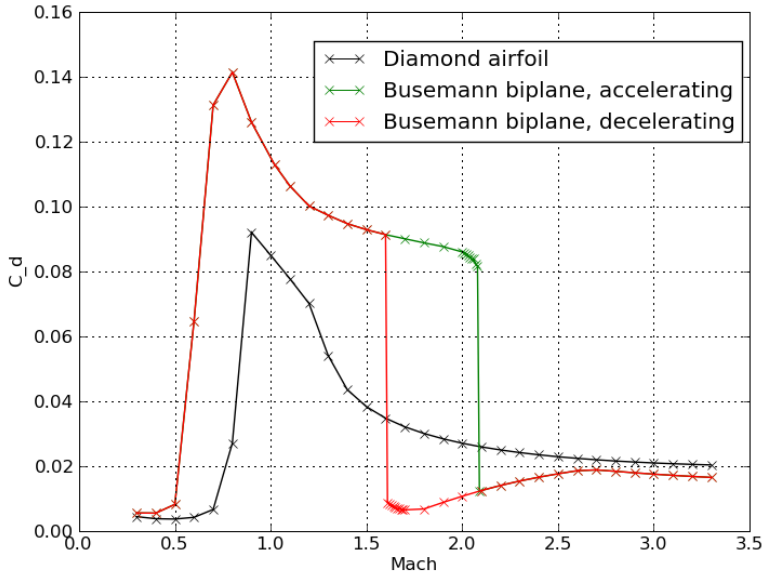

(b) $c_l = 0.1$

Figure 5.10: c_d plot of different airfoil under lifting condition

region between the two airfoils finally disappears. The flow-hysteresis phenomenon still exists as it does in the zero-lift condition. During deceleration,the wave drag is small (an order of magnitude) until a strong bow shock wave forms in front of the airfoil when the Mach number decreases due to the choked-flow effect.

In conclusion, similar to the zero-lift condition, the Busemann airfoil produces substantially lower wave drag than the standard diamond airfoil of the same thickness at Mach number 1.7 due to the favorable shock-shock interaction effect when c_l is fixed. However, the Busemann airfoil demonstrates poor off-design performance during acceleration and deceleration caused by the flow-hysteresis and choke-flow effect.

5.3.1 Optimized designs for lifting conditions

Just as in the zero-lift condition, multiple design points are used to optimize the biplane airfoil during acceleration and deceleration. A fixed thickness constraint is applied. The points at the maximum thickness section are fixed. The cost function is still the weighted c_d at all design points. Figure 5.11 shows the convergence history of these two design cases. From the plot, we can see the weighted sum is smallest at 550 design iterations for both cases. Therefore, we use the resulting airfoil after 550 design iterations as our optimized biplane airfoil.

The comparison of the drag coefficient for both cases are given in Table 5.5 and Table 5.6.

Mach	1.1	1.2	1.3	1.4	1.5	1.6	1.7	1.6	1.5	1.4	1.3	1.2	1.1
Baseline	1054	1000	962	934	913	896	881	896	913	934	962	1000	1054
Optimized	520	472	425	388	351	119	112	119	134	158	425	472	520

Table 5.5: c_d comparison for $c_l = 0.05$ (1 count = 0.0001)

Figure 5.12 shows a comparison of the optimized biplane airfoil with the original Busemann airfoil for both lift coefficients. As can be seen, the optimized biplane airfoil still has the same thickness as the original Busemann airfoil at all corresponding positions and the maximum thickness position is fixed by the constraints. Both the

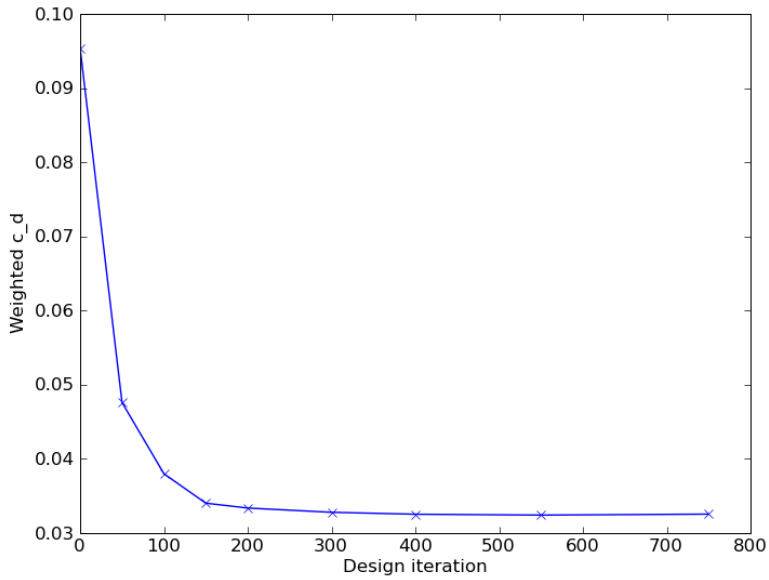

(a) $c_l = 0.05$

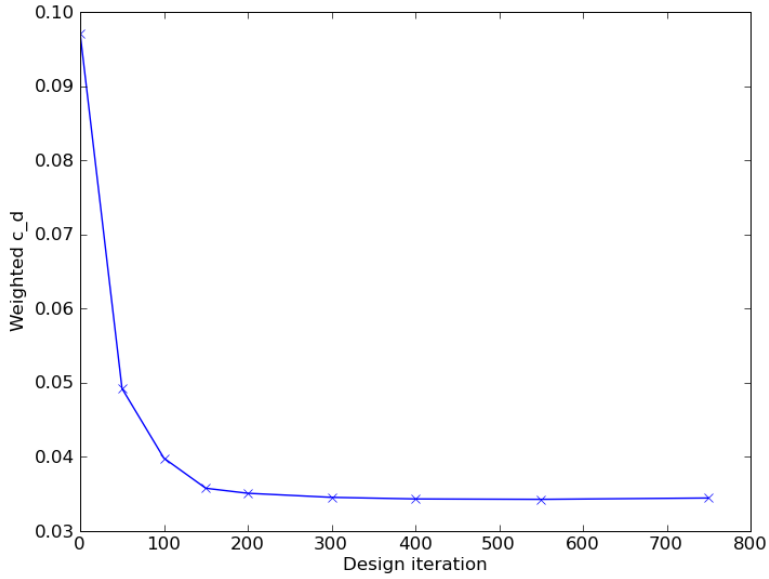

(b) $c_l = 0.1$

Figure 5.11: Convergence history under lifting conditions.

Mach	1.1	1.2	1.3	1.4	1.5	1.6	1.7	1.6	1.5	1.4	1.3	1.2	1.1
Baseline	1066	1013	977	952	933	918	905	918	933	952	977	1013	1066
Optimized	535	489	446	413	377	136	131	136	149	173	446	489	535

Table 5.6: c_d comparison for $c_l = 0.1$ (1 count = 0.0001)

leading edges and trailing edges of the optimized biplane airfoils bend towards the center. However, due to the lifting condition, the two components of the optimized airfoil are not symmetric.

Figure 5.13 shows the comparison of the drag coefficient for the optimized biplane airfoil with the standard diamond airfoil and the original Busemann airfoil at c_l = 0.05 and c_l = 0.1. Just as in the zero-lift condition, flow-hysteresis and choke-flow phenomenon still exist for the optimized Busemann airfoil. During acceleration, the wave drag of the optimized biplane airfoil is smaller than the wave drag of the original Busemann airfoil during the whole Mach number range (from 0.3 to 3.3). For deceleration, the wave drag of the optimized biplane airfoil is smaller than the wave drag of the original Busemann airfoil except for the Mach number range 1.6 to 2.1. Therefore, it is possible to greatly reduce the wave drag of the Busemann airfoil by using our multiple design point method.

The pressure coefficient distribution of the optimized biplane airfoil during acceleration and deceleration at c_l = 0.05 and c_l = 0.1 show the flow-hysteresis and choke-flow phenomenon are similar to the original Busemann airfoil. However, during acceleration, the bow shock wave is swallowed at a lower Mach number (Mach number 1.54). During deceleration, the optimized biplane airfoil shifts the choked flow at the maximum thickness section to a lower Mach number (Mach number 1.38).

5.4 Sensitivity Tests

To check whether the optimized biplane airfoil is robust for other off-design conditions, two sensitivity studies have been performed. The optimized biplane airfoil for zero lift is used in these studies.

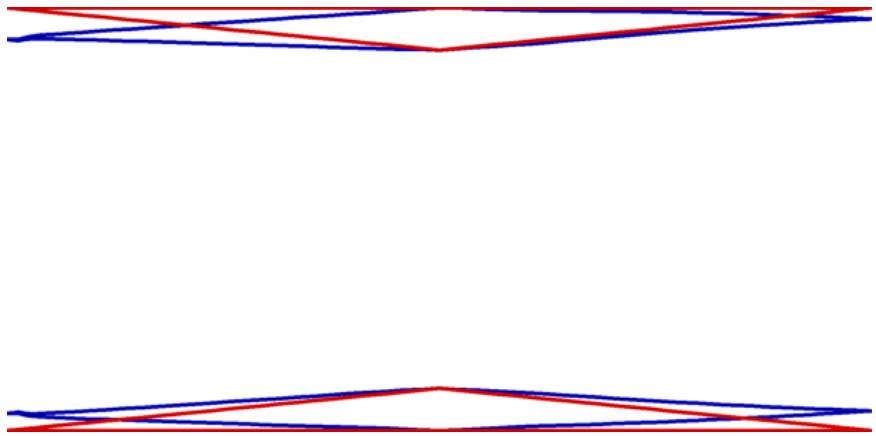

(a) $c_l = 0.05$

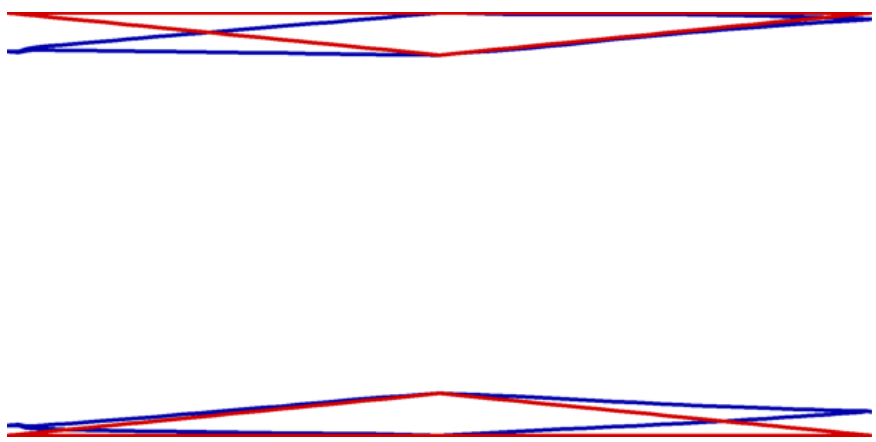

(b) $c_l = 0.1$

Figure 5.12: Comparison of baseline Busemann airfoil and the optimized biplane airfoil.

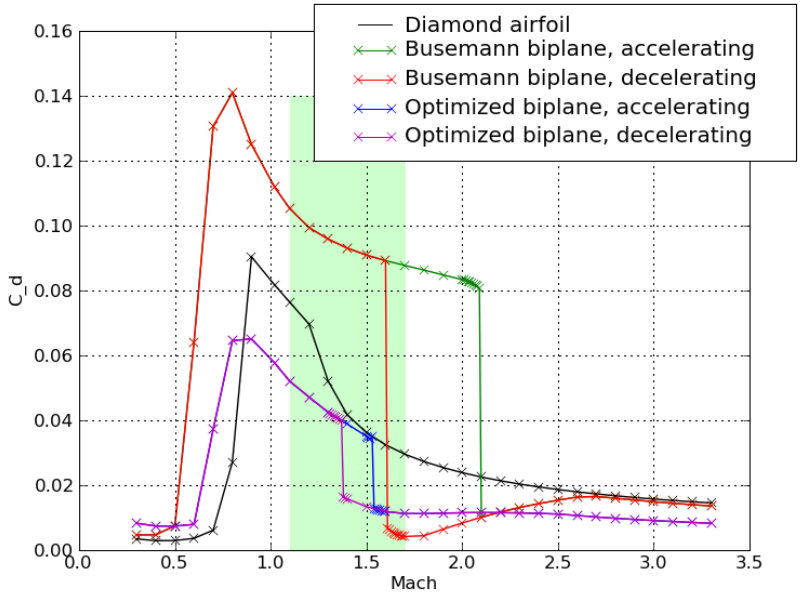

(a) $c_l = 0.05$

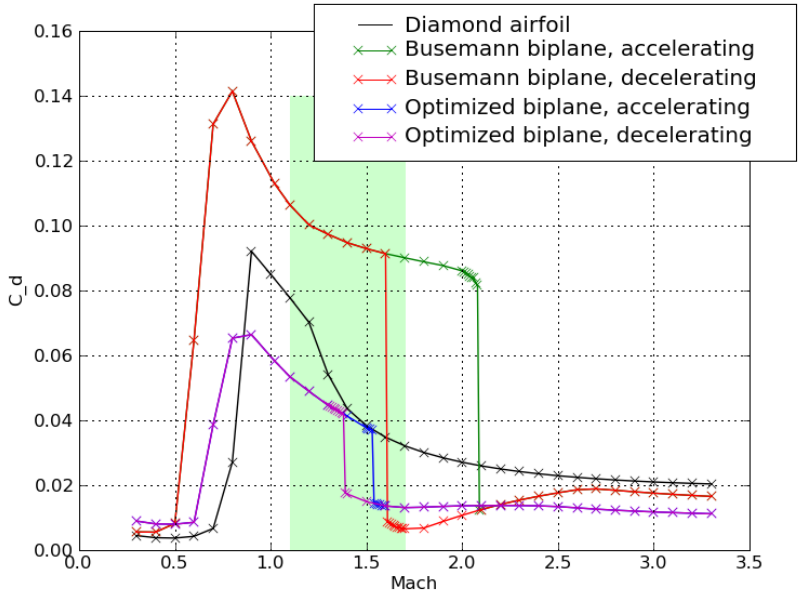

(b) $c_l = 0.1$

Figure 5.13: c_d plot of different airfoils under lifting condition.

Figure 5.14 shows the sensitivity to the angle of attack. In our simulation, the angle of attack is a uniform random number between 0 and 1 degree. Twenty-five different angle of attack conditions are tested. From the plot, we can see that the drag coefficient of the optimized biplane airfoil only change very small under all different angle of attack conditions. The flow hysteresis range (wave drag coefficient line splitting rang)for all cases are within 0.01 Mach number variation. Thus the optimized design is not very sensitive to the variation of the angle of attack.

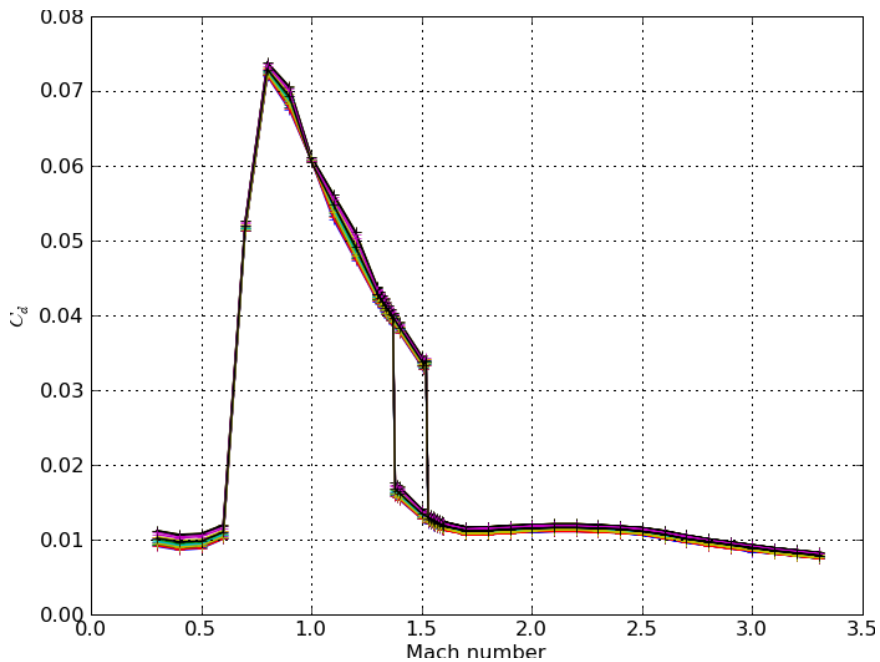

Figure 5.14: Sensitivity to angle of attack.

Figure 5.15 shows the sensitivity to the separation distance (the distance between two airfoils). The separation distance is a uniform random number between $\pm(0.02)$ chord length and again 25 different cases are tested. The separation distance of biplane airfoil is an important parameter because the shock wave from the leading edge will arrive different part of the opposite airfoil such that the pressure over the airfoil surface will change obviously. Thus we can see the wave drag in the Mach number range $(1.6, 2.5)$ for different cases are about 20% variation. For different separation distance cases, the flow will be unchoked at different Mach number. Thus the flow hysteresis ranges are not the same as the angle of attack sensitivity test.

When the Mach number is higher than 2.6, the shock wave from the leading edge will not interact with the opposite airfoil component. The wave drag for all different separation distance case will be the same.

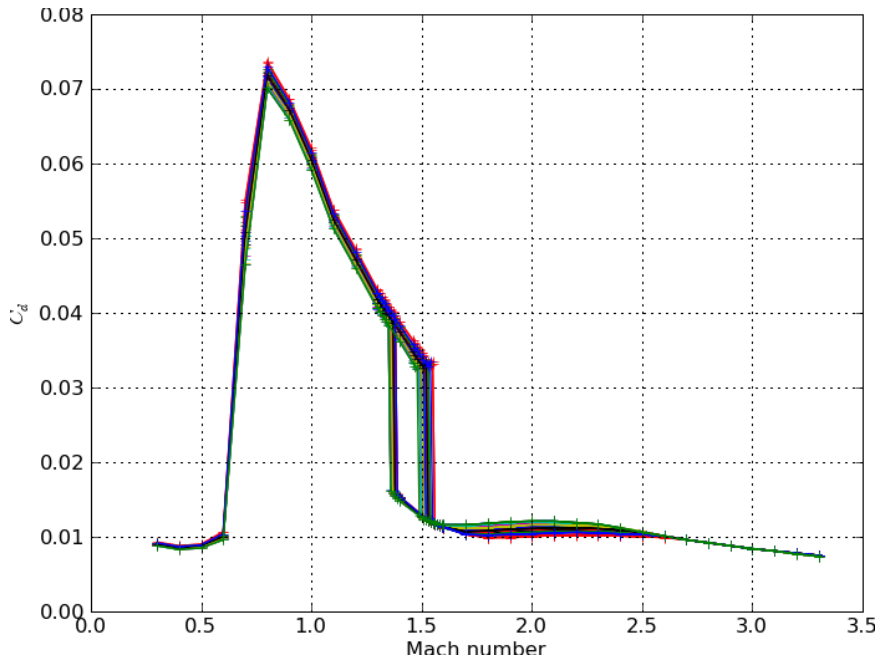

Figure 5.15: Sensitivity to separation distance.

5.5 Viscous Validation of the Optimized Airfoil

In previous sections, the inviscid Euler equations have been used as the govern equation to design the biplane airfoil. The results show that the optimized biplane can greatly reduce the wave drag due to the favorable shock wave interaction. However, it is important to remember that, compared with the standard diamond airfoil, the biplane airfoil design will increase the skin friction drag of the system because of the increased surface area. Since the design tool was based on Euler calculations, the viscous drag has been neglected. In this section, we validate the optimized biplane airfoil by solving the Navier-Stokes equations to show that the reduction in wave drag generally outweighs the increase in skin friction drag.

5.5.1 Navier-Stokes Equations Results

Here, the flow was modeled by the Reynolds Averaged Navier-Stokes equation, with a Baldwin Lomax turbulence model. Assume under previous flow conditions the flow is still attached, this turbulence model was considered sufficient. Similarly to in the inviscid case, 192×192 grid nodes are used and a zoom on the mesh is given in Figure 5.16. From the plot, we can see the aspect ratio of the mesh near the leading edge is really large. The large aspect ratio of the mesh and poor performance of the H-mesh at the leading edge cause a lot numerical difficulties for the flow calculation. Since the Reynolds number is proportional to the velocity, the Reynolds numbers in the calculation is set to $Mach \times 10^6$.

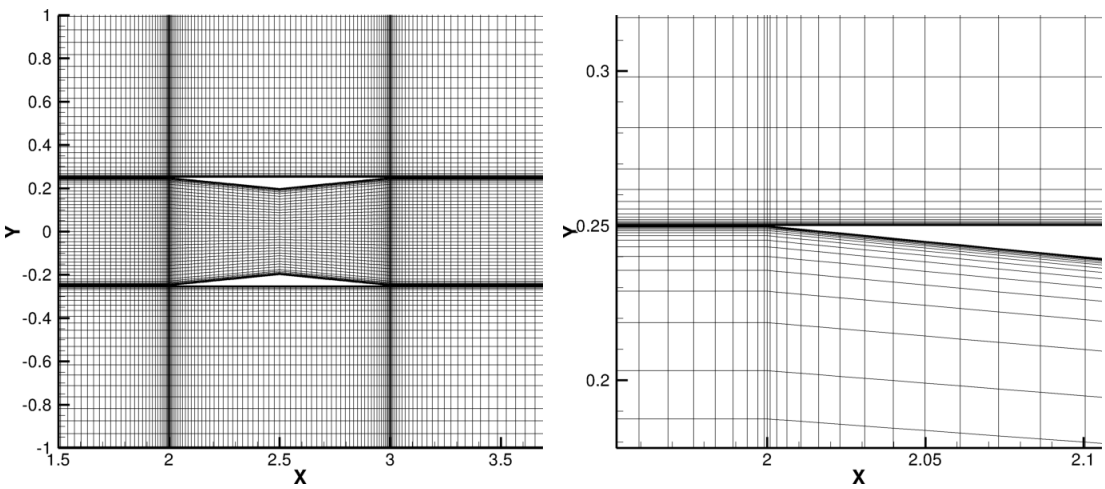

(a) Zoom 1

(b) Zoom 2

Figure 5.16: Viscous mesh

A comparison of drag coefficients versus Mach number is given in Figure 5.17 for zero lift condition and lifting ($cl = 0.05$) condition. In the plot, all the dashed lines are the Euler results and the solid lines are Navier-Stokes results. Just as in the inviscid cases, we can see the zero-lift condition and the lifting condition results are similar. Since no separation occurred, the drag difference between the Navier-Stokes results and Euler results is mainly skin friction drag. Accordingly the skin friction drag of

optimized biplane is almost twice that of the standard diamond airfoil. From the plot, we can see, except for a very small Mach number range (about 1.4 to 1.5 during acceleration), the total drag of the optimized biplane airfoil is smaller than that of the standard diamond airfoil. The flow hysteresis area of the biplane changed a little due to the boundary layer. Considering the boundary layer, ratio of the leading edge to maximum thickness points decrease such that the flow hysteresis range shift to a higher Mach number. But this change is very small and the flow hysteresis area is still very small compared to the baseline Busemann airfoil.

5.5.2 Flat Plate Approximation

Because of the high aspect ratio of the mesh and the sharp leading edge property of our problem, it is difficult to increase the Reynolds number for our calculation. But for the real case, a Reynolds number equal 10^6 is not high enough. Since we assume no flow separation and the total drag of the airfoil is only due to the inviscid drag and the skin friction drag, we use a flat plate approximation for the higher Reynolds numbers cases here. The procedure for this flat plate approximation is,

1. Calculate drag of a flat plate under zero angle of attack at given Reynolds number, c_f;
2. Add c_f to the inviscid drag of the standard diamond airfoil;
3. Add $2 \times c_f$ to the inviscid drag of the optimized biplane airfoil;
4. Compare above two results.

Before we increase the Reynolds number, we first did a comparison of the N-S results with the flat plate approximation results at Reynolds number 10^6. The results are given in Figure 5.18. In the plot, all the dash lines are the N-S results and the solid lines are flat plate approximation results. We can see from the plot, the results obtained by these two methods are in good agreement.

Figure 5.19 and Figure 5.20 show the comparison of the drag coefficient versus Mach number with Reynolds number equal $Mach \times 8 \times 10^6$ and $Mach \times 2 \times 10^7$

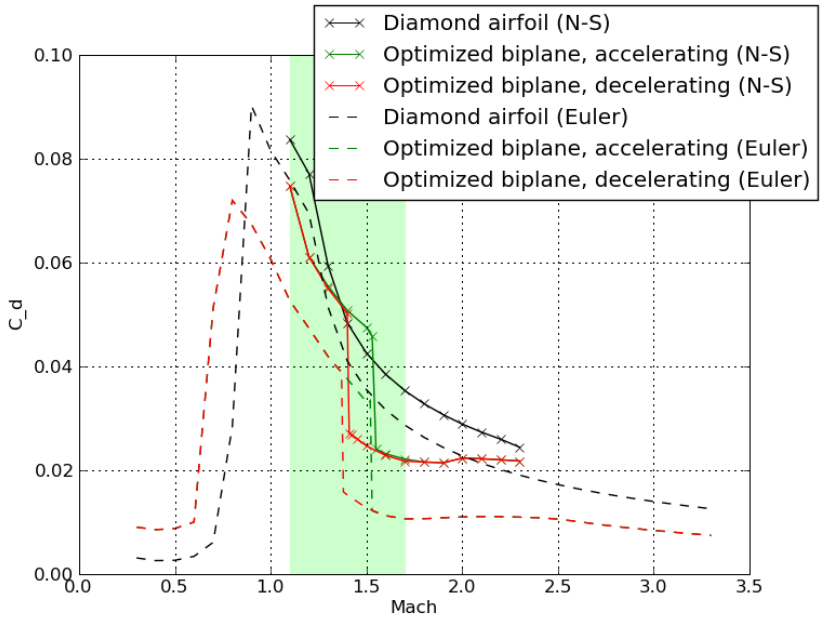

(a) Zero Lift

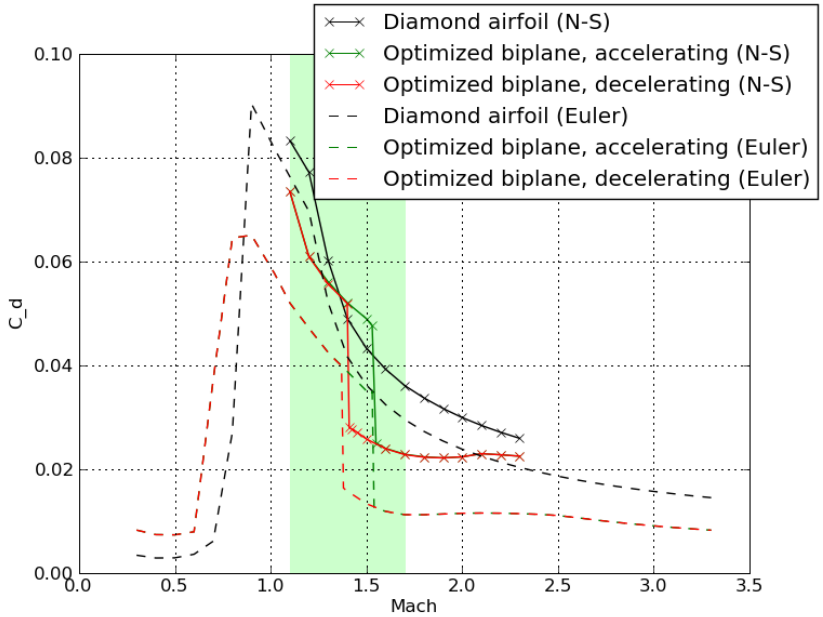

(b) $c_l = 0.05$

Figure 5.17: Comparison of drag coefficients by Navier-Stokes Equations

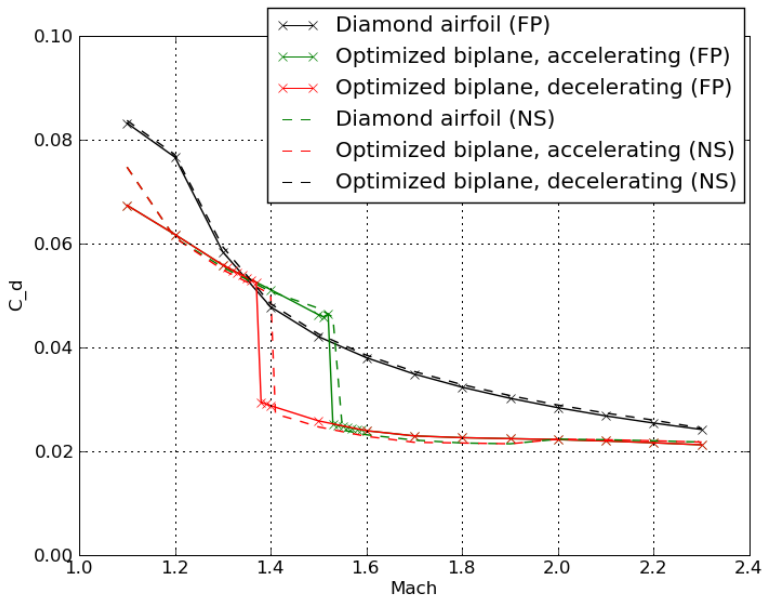

Figure 5.18: N-S results and flat plate approximation results comparison

respectively under zero lift condition and lifting ($c_l = 0.05$) condition by using flat plate approximation. From both plots, we can see the optimized biplane airfoil has lower drag for almost all the Mach number range except a very small region (around 1.4 to 1.5 during acceleration) than that of the standard diamond airfoil. Since now the total drag is just a summation of the inviscid drag (wave drag here) and the skin friction drag, the flow hysteresis region for the optimized biplane airfoil does not change.

We can see that the increase in skin friction drag caused by biplane is smaller than the decrease in wave drag due to the favorable shock wave interaction, as shown by both the Navier-Stokes equations results and flat plate approximation results in this section. Consequently the optimized biplane airfoils obtained by the inviscid design method produces lower drag than the standard diamond airfoil over most of the optimization Mach number range.

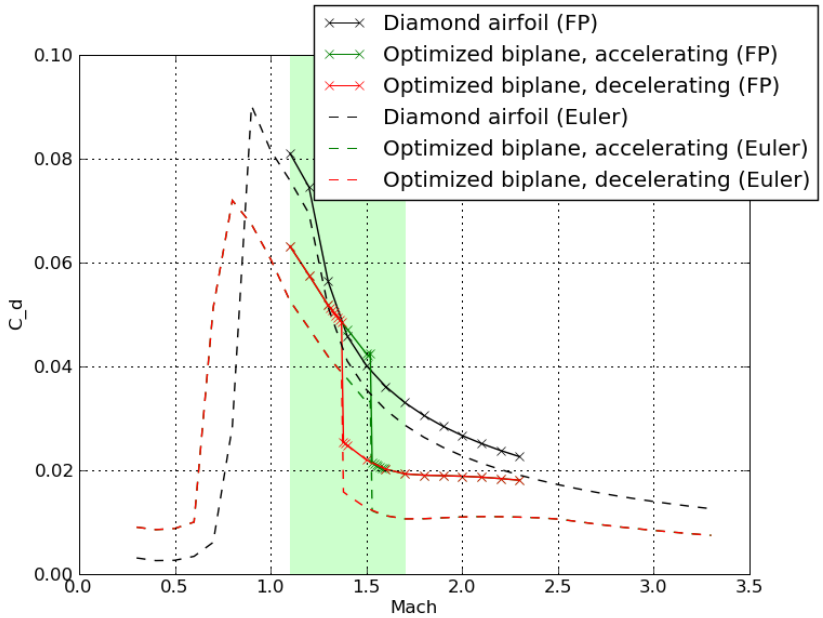

(a) Zero Lift

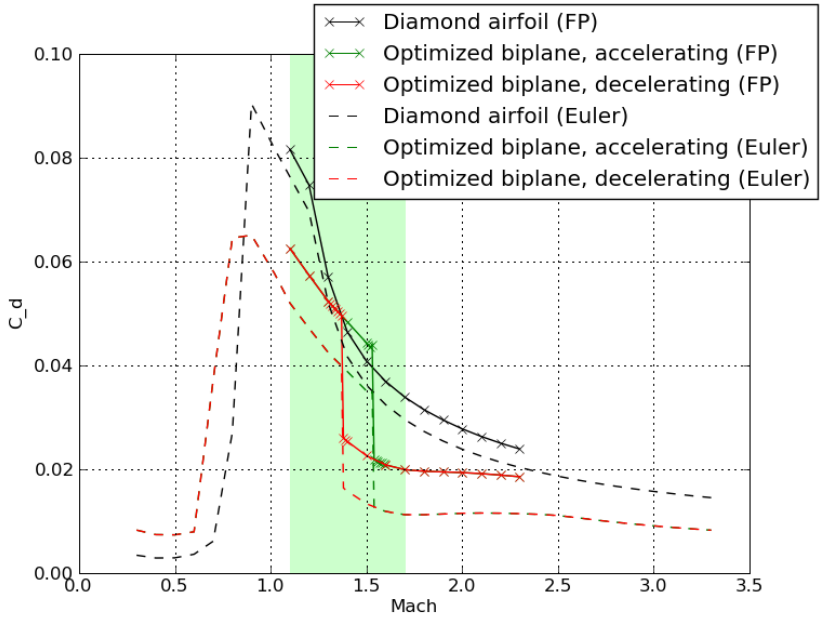

(b) $c_l = 0.05$

Figure 5.19: Comparison of drag coefficients by flat plate approximation (Re=8E6)

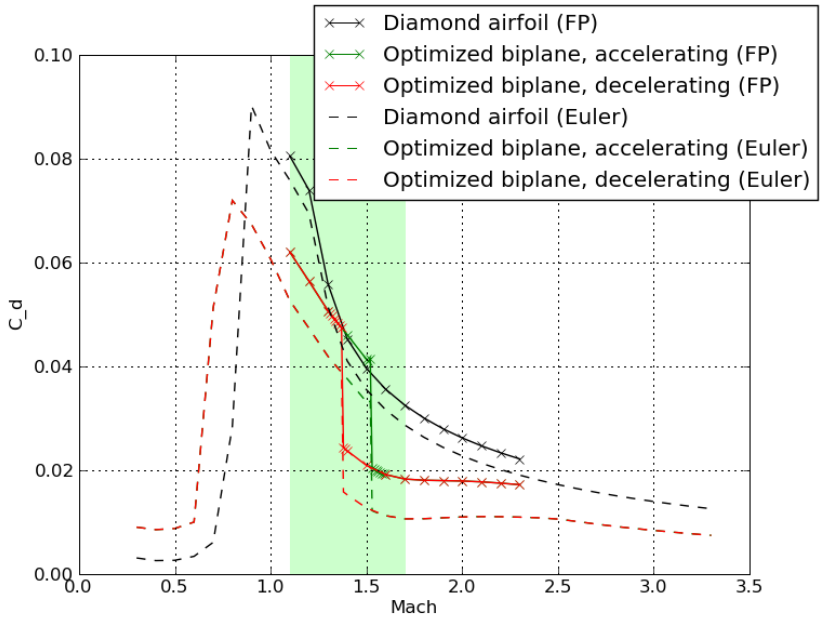

(a) Zero Lift

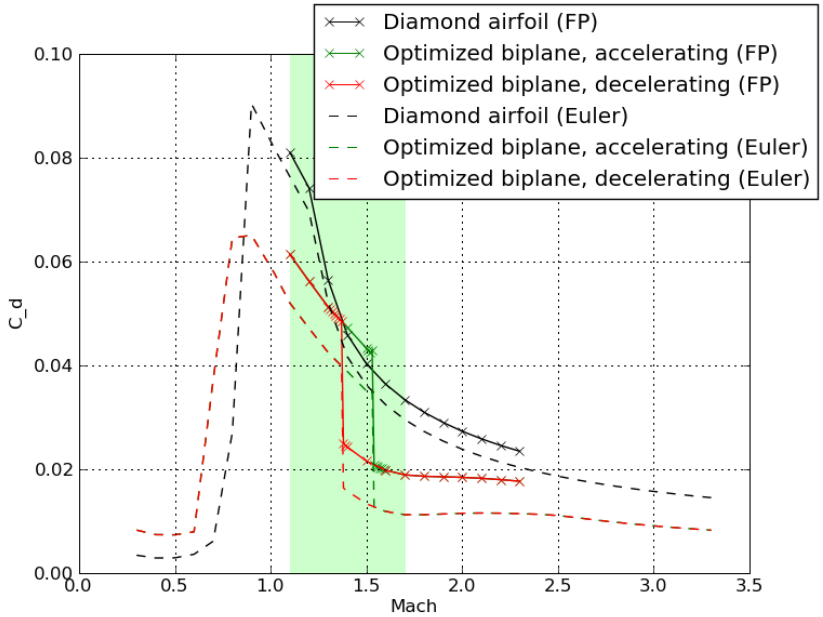

(b) $c_l = 0.05$

Figure 5.20: Comparison of drag coefficients by flat plate approximation (Re=2E7)

Chapter 6

Conclusion and Future Work

In this dissertation the favorable shock wave interaction of the supersonic biplane airfoil is studied. Two-dimensional numerical simulation results show that the Busemann biplane airfoil produces very low wave drag under design condition due to the perfect shock-expansion wave cancellation. But for off-design conditions, the Busemann biplane airfoil performance is poor. To overcome the choked-flow and flow-hysteresis problems of the Busemann biplane under off-design conditions, the inviscid compressible flow (Euler) optimization techniques based on control theory have been applied.

In order to obtain an optimized supersonic airfoil with lower wave drag within the given optimization Mach number range, a multiple design point strategy is employed. The optimized biplane airfoil shows good performance under both design and off-design conditions. The flow-hysteresis phenomenon of the optimized airfoil still exists but the area is greatly reduced compared to that of the baseline Busemann biplane and the wave drag caused by choked flow is also much lower. For inviscid flow, the wave drag of the optimized biplane airfoil is lower than that of the diamond airfoil with the same total thickness throughout the optimization range. The two sensitivity studies show that the optimized design is robust and not very sensitive to the change of the angle of attack or the separation distance.

According to both the Navier-Stokes equations results and flat plate approximation results, the increase in skin friction drag caused by biplane is smaller than the

decrease in wave drag due to the favorable shock wave interaction. The optimized biplane airfoils obtained by inviscid design method produce lower drag than the standard diamond airfoil over almost all the optimization Mach number conditions except for a small Mach number range during acceleration.

The supersonic biplane airfoil design in this dissertation has demonstrated the successful application of the adjoint based optimization method to reduce wave drag and also the sonic boom by introducing the favorable shock wave interaction. However, the aerodynamic optimization has only been performed for two-dimensional inviscid flow conditions. Two future research topics should be pursued: three-dimensional design and viscous design. Also the shock / boundary layer interaction should be further studied and addressed. An unstructured mesh should be used to do viscous design since the H-type mesh in this research has been proved not very good for the viscous condition. Also a more practical leading edge and integration of biplane wings to fuselages will be interesting topics for future research. In addition, this kind of airfoil should be studied for an entire flight profile, including take-off and landing conditions, where the Mach number is low and c_l is high. Also, studies should be done to show that a biplane design can reduce or at least not increase structural weight, when the total thickness is the same as a monoplane. Another aspect is control and stability. Traditional analysis should remain valid in subsonic and unchoked supersonic flight, but the implications of the choked transonic and supersonic flight regimes for the stability of the airplane present an interesting challenge for future study.

Bibliography

[1] 2001 *Commercial Supersonic Technology: the Way Ahead / Committee on Breakthrough Technology for Commercial Supersonic Aircraft , Aeronautics and Space Engineering Board, Division on Engineering and Physical Sciences, National Research Council*. Washington, D.C.: National Academy Press.

[2] Aeronautics, NASA (National & Administration), Space 1998 Nasa technology plan. `http://technologyplan.nasa.gov/default.cfm?id=1.0`; Accessed on September 13, 2001.

[3] A.Jameson 1974 Iterative solution of transonic flows over airfoils and wings, including flows at mach 1. *Comm. Pure. Appl. Math* **27**, 283–309.

[4] Brandt, A. 1977 Multi-level adaptive solutions to boundary value problems. *Math Comput* **31**, 333–90.

[5] Busemann, A. 1935 *Aerodynamic Lift at Supersonic Speeds*, 12th edn., pp. 210–220. Luftfahrtforschung.

[6] Council), NRC (National Research 1997 U.s. supersonic commercial aircraft. `http://www.nap.edu/catalog/5848.html`; Accessed on October 23, 2008.

[7] David, L. 2000 Laser-boosted rocket sets altitude record. Space.com, `http://www.space.com/businesstechnology/technology/laser_craft_001103.html`; Accessed on October 22, 2008.

[8] Fedorenko, R.P. 1962 A relaxation method for solving elliptic differential equations. *USSR Computational Math. and Math. Phys.* **1**, 1092–6.

[9] Fedorenko, R.P. 1964 The speed of convergence of one iterative process. *USSR Computational Math. and Math. Phys.* **4**, 227–235.

[10] Ferri, A. 1949 *Elements of aerodynamics of supersonic flow*. New York: The Macmillan Company, also published from Dover Phoenix Edition,Dover Publications, Inc., New York, 2005.

[11] Garabedian, P. R. & Korn, D. G. 1971 Numerical design of transonic airfoils. *Proceedings of SYNSPADE 1970* pp. 253–271.

[12] Gear, C.W. 1971 *Numerical Initial Value Problems*. Englewood Cliffs: Prentice Hall.

[13] George, F. 2000 The supersonic business jet. *Business and Commercial Aviation* pp. 44–48.

[14] Goto, Y., Kusunose, K., Yamashita, H. & Yonezawao, M. 2004 Numerical analysis of busemann's biplane for application to boomless supersonic transport. In *JSME 17th Computational Mechanics Conference*, pp. 117–118. Sendai, Japan.

[15] Hackbusch, W. 1978 On the multi-grid method applied to difference equations. *Computing* **20**, 291–306.

[16] Henne, P. A. 1980 An inverse transonic wing design method. AIAA paper 80–0330.

[17] Hicks, R. M. & Henne, P. A. 1979 Wing design by numerical optimization. AIAA paper 79–0080.

[18] Hicks, R. M., Murman, E. M. & Vanderplaats, G. N. 1979 An assessment of airfoil design by numerical optimization. Ames Research Center, Moffett Field, California: NASA TM X-3092.

[19] Hirsch, C. 1988 *Numerical Computation of Internal and External Flows*, , vol. 1. New York: John Wiley & Sons.

[20] der Houwen, Van 1977 *Construction of Integration Formulas for Initial Value Problems*. Amsterdam, Holland: North-Holland.

[21] Igra, D. & Arad, E. 2007 A parametric study of the busemann biplane phenomena. *Shock Waves* **16** (33), 269–273.

[22] Jameson, A. 1982 Steady state solution of the euler equations for transonic flow. In *In Proceedings of Symposium on Transonic, Shock and Multidimensional Flows* (ed. R. Meyer), pp. 30–37. Madison, WI: Academic Press.

[23] Jameson, A. 1983 Solution of the euler equations for two dimensional transonic flow by a multigrid method. *Applied Mathematics and Computations* **13**, 327–356.

[24] Jameson, A. 1985 Multigrid algorithms for compressible flow calculations. In *Proceedings of the 2nd European Conference on Multigrid Methods*. Cologne: Princeton University Report MAE 1743.

[25] Jameson, A. 1988 Aerodynamic design via control theory. *Journal of Scientific Computing* **3**, 233–260, also, Princeton University Report MAE 1824, ICASE Report No. 88-64, November 1988.

[26] Jameson, A. 1995 Optimum aerodynamic design using CFD and control theory. In *AIAA 12th Computational Fluid Dynamics Conference*. San Diego, CA: AIAA paper 95–1729.

[27] Jameson, A. & Baker, T.J. 1983 Solution of the euler equations for complex configurations. In *AIAA 6th Computational Fluid Dynamics Conference*. Danvers, MA: AIAA paper 83–1929.

[28] Jameson, A., Baker, T.J. & Weatherill, N.P. 1986 Calculation of inviscid transonic flow over a complete aircraft. In *AIAA 24th Aerospace Sciences Meeting*. Reno: AIAA paper 86–0103.

[29] Jameson, A. & Caughey, D.A. 1977 A finite volume method for transonic potential flow calculations. In *AIAA 3rd Computational Fluid Dynamics Conference*, pp. 35–54. Albuquerque.

[30] Jameson, A. & Martinelli, L. 2000 Aerodynamic shape optimization techniques based on control theory. In *CIME Summer Course on Computational Mathematics Driven by Industrial Problems* (ed. V Capasso, H. Engl & J. Periaux), *Lecture Notes in Mathematics*, vol. 1739. Martina Franca, Italy: Springer.

[31] Jameson, A., Martinelli, L. & Pierce, N. 1997 Optimum aerodynamic design using the Navier-Stokes equations. In *35th Aerospace Sciences Meeting and Exhibit*. Reno, Nevada: AIAA paper 97–0101.

[32] Jameson, A., Martinelli, L. & Pierce, N. 1998 Optimum aerodynamic design using the Navier-Stokes equations. *Theoretical Computational Fluid Dynamics* **10**, 213–237.

[33] Jameson, A., Schmidt, W. & Turkel, E. 1981 Numerical solutions of the euler equations by finite volume methods with runge-kutta time stepping schemes. AIAA paper 81-1259.

[34] Kashitani, M., Yamaguchi, Y., Kai, Y. & Hirata, K. 2008 Preliminary study on lift coefficient of biplane airfoil in smoke wind tunnel. In *46th AIAA Aerospace Sciences Meeting and Exhibit*. AIAA 2008-349.

[35] Kuratani, N., Ogawa, T., Yamashita, H., Yonezawa, M. & Obayashi, S. 2007 Experimental and computational fluid dynamics around supersonic biplane for sonic-boom reduction. In *13th AIAA/CEAS Aeroacoustics Conference (28th AIAA Aeroacoustics Conference)*. AIAA 2007-3674.

[36] Kusunnose, K. ???? A wake integration method for airplane drag prediction. *The 21st Century COE Program International COE of Flow Dynamics Lecture Series* **3**, 65–70.

[37] Kusunose, K., Matsushima, K., Goto, Y., Yamashita, H., Yonezawa, M., Maruyama, D. & Nakano, T. 2006 A fundamental study for the development of boomless supersonic transport aircraft. In *44rd AIAA Aerospace Sciences Meeting and Exhibit*. AIAA 2006-654.

[38] Kusunose, K., Yonezawa, M., Obayashi, S. & Kusunose, K. 2007 A study of busemann-type biplane for avoiding choked flow. In *45th AIAA Aerospace Sciences Meeting and Exhibit*. Reno, Nevada: AIAA 2007-688.

[39] Lambert, J.D. 1991 *Numerical Methods for Ordinary Differential Systems: the Initial Value Problem*. Chichester, NY: Wiley.

[40] Leoviriyakit, K. & Jameson, A. 2005 Multi-point wing planform optimization via control theory. In *43rd AIAA Aerospace Sciences Meeting and Exhibit*. Reno, NV: AIAA Paper 2005-0450.

[41] Licher, R.M. 1955 Optimum two-dimensional multiplanes in supersonic flow. *Tech. Rep.* SM-18688. Douglass Aircraft Co.

[42] Liepmann, H.W. & Roshko, A. 1957 *Elements of Gasdynamics*, chap. Waves in Supersonic Flow, pp. 107–118. Mineola, New York: Dover Publications, Inc.

[43] Lighthill, M. J. 1945 A new method of two dimensional aerodynamic design. *ARC, Rand M 2112* .

[44] Lions, J. L. 1971 *Optimal Control of Systems Governed by Partial Differential Equations*. New York: Springer-Verlag, translated by S. K. Mitter.

[45] Lynch, F.T. 1982 *Transonic aerodynamics*, *Progress in Astronautics and Aeronautics*, vol. 81, chap. Commercial Transports - Aerodynamic Design for Cruise Performance Efficiency, pp. 81–144. New York: AIAA.

[46] MacCormack, R.W. 1985 Current status of numerical solutions of the navier-stokes equations. In *AIAA 23rd Aerospace Sciences Meeting*. Reno: AIAA paper 85–0032.

[47] Martinelli, L. 1987 Calculations of viscous flow with a multigrid method. PhD thesis, Princeton University, Princeton, NJ.

[48] Maruyama, D., Matsushima, K., Kusunose, K. & Nakahashi, K. 2006 Aerodynamic design of biplane airfoils for low wave drag supersonic flight. In *24th Applied Aerodynamics Conference*. San Francisco, California: AIAA 2006–3323.

[49] Maruyama, D., Matsuzawa, T., Kusunose, K., Matsushima, K. & Nakahashi, K. 2007 Consideration at off-design conditions of supersonic flows around biplane airfoils. In *45th AIAA Aerospace Sciences Meeting and Exhibit*. AIAA 2007-687.

[50] McFadden, G. B. 1970 An artificial viscosity method for the design of supercritical airfoils. *Tech. Rep.* C00-3077-158. New York University.

[51] Moeckel, W. E. 1947 Theoretical aerodynamic coefficients of the two-dimensional supersonic biplane. *Tech. Rep.* 1316. NACA.

[52] Murman, E.M. & Cole, J.D. 1971 Calculation of plane steady transonic flows. *AIAA Journal* **9**, 114–121.

[53] Neumann, J. Von & Richtmyer, R.D. 1950 A method for the numerical calculations of hydrodynamical shocks. *Journal Mathematical Physics* **21**.

[54] Ni, R.H. 1982 A multiple grid scheme for solving the euler equations. *AIAA Journal* **20**, 1565–1571.

[55] Pawlowski, J.W., Graham, D.H. & Boccadoro, C.H. 2005 Origins and overview of the shaped sonic boom demonstration program. In *43rd AIAA Aerospace Sciences Meeting and Exhibit*. AIAA 2005-5.

[56] Pulliam, T.H. & Steger, J.L. 1985 Recent improvements in efficiency, accuracy and convergence for implicit approximate factorization algorithms. In *AIAA 23rd Aerospace Sciences Meeting*. Reno: AIAA paper 85–0360.

[57] Reuther, J. & Jameson, A. 1995 Aerodynamic shape optimization of wing and wing-body configurations using using control theory. In *33rd Aerospace Sciences Meeting and Exhibit*. Reno, Nevada: AIAA paper 95–0123.

[58] Science, NSTC (National, Technology Council)Committee on Technology, Subcommittee on Transportation Research & Development 2000 National transportation strategic research plan. `http://www.volpe.dot.gov/infosrc/strtplns/nstc/srplan00/index.html`; Accessed on September 13, 2001.

[59] Shankaran, S. & Jameson, A. 2003 Numerical analysis and design of upwind sails. In *21st AIAA Applied Aerodynamics Conference*. Orlando, FL: AIAA Paper 2003-3531.

[60] Tan, H. S. 1950 The aerodynamics of supersonic biplanes of finite span. *Tech. Rep.* 52-276. WADC.

[61] Tranen, J. L. 1974 A rapid computer aided transonic airfoil design method. AIAA paper 74–5017.

[62] of Transportation), DOT (Department 1999 Effective global transportation in the twenty-first century: A vision document. u.s. department of transportation research and technology coordinating council. `http://www.volpe.dot.gov/infosrc/strtplns/dot/glbtrn21/index.html#toc`; Accessed on September 13, 2001.